

1 Chemogenomic profiling of anti-leishmanial efficacy and resistance in the
2 related kinetoplastid parasite *Trypanosoma brucei*

3

4 Clare F Collett ^{a,*}, Carl Kitson ^a, Nicola Baker ^{b,*}, Heather B. Steele-Stallard ^a, Marie-
5 Victoire Santrot ^{a,*}, Sebastian Hutchinson ^{b,*}, David Horn ^b, Sam Alford ^{a,#}

6

7 ^a London School of Hygiene and Tropical Medicine, Keppel Street, London WC1E 7HT,
8 United Kingdom

9 ^b Wellcome Trust Centre for Anti-Infectives Research, School of Life Sciences, University
10 of Dundee, Dundee DD1 5EH, United Kingdom.

11

12 Running Head: Anti-leishmanial drug efficacy determinants

13

14 # Address correspondence to sam.alsford@lshtm.ac.uk

15

16 * Present address: Clare Collett, School of Biological Sciences, University of Bristol,
17 Bristol, United Kingdom; Nicola Baker, Department of Biology, University of York,
18 Heslington, York, United Kingdom; Sebastian Hutchinson, Trypanosome Cell Biology,
19 Institut Pasteur, Paris, France

20

21

22 Word counts:

23 Abstract, 217; importance, 135

24 Main text (intro, results, discussion), 4953.

25 **Abstract**

26 The arsenal of drugs used to treat leishmaniasis, caused by *Leishmania* spp., is limited
27 and beset by toxicity and emergent resistance. Furthermore, our understanding of drug
28 mode-of-action and potential routes to resistance is limited. Forward genetic approaches
29 have revolutionised our understanding of drug mode-of-action in the related kinetoplastid
30 parasite, *Trypanosoma brucei*. Therefore, we screened our genome-scale *T. brucei* RNAi
31 library in the current anti-leishmanial drugs, sodium stibogluconate (antimonial),
32 paromomycin, miltefosine and amphotericin-B. Identification of *T. brucei* orthologues of the
33 known *Leishmania* antimonial and miltefosine plasma membrane transporters effectively
34 validated our approach, while a cohort of 42 novel drug efficacy determinants provides
35 new insights and serves as a resource. Follow-up analyses revealed the antimonial
36 selectivity of the aquaglyceroporin, TbAQP3. A lysosomal major facilitator superfamily
37 transporter contributes to paromomycin/aminoglycoside efficacy. The vesicle-associated
38 membrane protein, TbVAMP7B, and a flippase contribute to amphotericin-B and
39 miltefosine action, and are potential cross-resistance determinants. Finally, multiple
40 phospholipid-transporting flippases, including the *T. brucei* orthologue of the *Leishmania*
41 miltefosine transporter, a putative β -subunit/CDC50 co-factor, and additional membrane-
42 associated hits, affect amphotericin-B efficacy, providing new insights into mechanisms of
43 drug uptake and action. The findings from this orthology-based chemogenomic profiling
44 approach substantially advance our understanding of anti-leishmanial drug action and
45 potential resistance mechanisms, and should facilitate the development of improved
46 therapies, as well as surveillance for drug-resistant parasites.

47 **Importance**

48 Leishmaniasis is a devastating disease caused by the *Leishmania* parasites and is
49 endemic to a wide swathe of the tropics and sub-tropics. While there are drugs available
50 for the treatment of leishmaniasis, these suffer from various challenges, including the
51 spread of drug resistance. Our understanding of anti-leishmanial drug action and the
52 modes of drug resistance in *Leishmania* is limited. The development of genetic screening
53 tools in the related parasite, *Trypanosoma brucei*, has revolutionised our understanding of
54 these processes in this parasite. Therefore, we applied these tools to the anti-leishmanial
55 drugs, identifying *T. brucei* orthologues of known *Leishmania* proteins that drive drug
56 uptake, as well as a panel of novel proteins not previously associated with anti-leishmanial
57 drug action. Our findings substantially advance our understanding of anti-leishmanial
58 mode-of-action and provide a valuable starting point for further research.

59 Introduction

60 The kinetoplastid parasites, *Leishmania* species, *Trypanosoma brucei* subspecies
61 and *T. cruzi* are respectively endemic throughout much of the tropics and sub-tropics, sub-
62 Saharan Africa and Latin America. They are responsible for various forms of leishmaniasis
63 (*Leishmania* spp.) (1), human African trypanosomiasis (HAT; *T. b. gambiense* and *T. b.*
64 *rhodesiense*) and the livestock disease, nagana (*T. b. brucei* and related African
65 trypanosomes) (2), and Chagas' disease (*T. cruzi*) (3). Collectively, these parasites cause
66 a huge burden of disease amongst predominantly poor populations in affected regions.
67 Leishmaniasis is caused by a range of *Leishmania* species, leading to cutaneous and
68 visceral forms of the disease, of which there are 0.7-1.3 and 0.2-0.4 million cases annually
69 (4). While cutaneous leishmaniasis can be self-limiting, infections with *L. braziliensis* (and
70 other members of the *Viannia* sub-genus) can develop into mucocutaneous leishmaniasis,
71 a profoundly disfiguring form of the disease (4). Visceral leishmaniasis, also known as
72 kala-azar, is typically fatal if untreated.

73 There are four current anti-leishmanial drugs: sodium stibogluconate (SSG),
74 paromomycin, miltefosine and amphotericin-B, which are unsatisfactory due to toxicity,
75 emerging drug resistance, complex administration protocols and variable efficacy
76 depending on the disease type or infecting *Leishmania* species (5). With the exception of
77 miltefosine (in use against leishmaniasis since 2002), the current anti-leishmanial drugs
78 have been in use for many decades. Until recently, efforts have focused on the
79 development of more effective drug delivery regimens and combination therapies, with the
80 aim of reducing dosages (and therefore side effects) and combating the emergence of
81 resistance. The rise of antimonial resistant *L. donovani* on the Indian sub-continent now
82 precludes the use of sodium stibogluconate (SSG) (6), while miltefosine resistant *L.*
83 *donovani* has been confirmed in the clinic (7). Consequently, the World Health
84 Organisation recommends various combination therapies, depending on the *Leishmania*

85 species and geographical region (8). However, it is relatively easy to generate *Leishmania*
86 resistant to combination therapies in the laboratory (9, 10). More recently, new drugs have
87 entered the clinical development pipeline. However, the most advanced of these,
88 fexinidazole, which recently passed phase 2/3 clinical trials against HAT (11), and has
89 anti-leishmanial activity *in vitro* (12), lacks efficacy *in vivo* (13).

90 Given the ease with which *Leishmania* parasites become resistant to the available
91 drugs, it is critically important to understand how this resistance might develop.
92 Identification of the genetic changes underlying drug resistance will enable the
93 development of molecular diagnostics to inform treatment choice (14). *Leishmania*
94 genome and transcriptome analyses have identified large numbers of candidate genes
95 (15, 16) but relatively few have been directly linked to drug-action. While some drugs can
96 freely move across membranes, many are taken up *via* specific surface receptors and
97 transporters. For example, miltefosine uptake is dependent on a *Leishmania* amino
98 phospholipid-transporting (P4)-type ATPase (or flippase) and its β -subunit/CDC50 co-
99 factor, Ros3 (17, 18), while the Sb(III) form of SSG is taken up *via* an aquaglyceroporin,
100 AQP1 (19). There is also evidence that the ABC transporter, MRPA, influences SSG
101 uptake and sequestration (20), and several other proteins have been implicated in SSG
102 efficacy (reviewed in (14)). In addition, the generation of drug resistant *Leishmania* in the
103 laboratory and various 'omics analyses have provided insights into anti-leishmanial drug
104 action and resistance mechanisms. Proteomic analyses of paromomycin resistant *L.*
105 *donovani* revealed a complex picture, with a range of proteins upregulated, including
106 several involved in translation regulation, vesicular trafficking and glycolysis (21). A similar
107 analysis of amphotericin-B resistant *L. infantum* highlighted the differential expression of
108 metabolic enzymes and the upregulation of proteins involved in protection against reactive
109 oxygen species (22). Metabolomic analyses suggested that oxidative defence also
110 contributes to SSG/amphotericin-B and SSG/paromomycin resistance in *L. donovani* (23).

111 The studies described above highlight the phenotypic consequences of changes in
112 drug sensitivity, but not necessarily the genetic changes responsible. Forward genetic
113 approaches can identify genes that contribute to drug action and resistance. For example,
114 genome-scale RNAi library screening, coupled with RNA interference target sequencing
115 (RIT-seq), has revolutionised our understanding of anti-HAT drug action and resistance
116 (24, 25). In addition, the Cos-seq approach has enabled gain-of-function screening in
117 *Leishmania* (26), leading to target validation for *N*-myristoyltransferase (27) and the
118 identification of a panel of putative antimony and miltefosine resistance genes (28). While
119 undoubtedly a powerful technique, Cos-seq is unable to identify drug uptake or activation
120 mechanisms, which can be characterised by loss-of-function approaches, such as RIT-
121 seq. However, due to the absence of the RNAi machinery in most *Leishmania* species
122 (with the notable exception of *L. braziliensis* (29)), this loss-of-function approach is not
123 possible in these parasites. Although *T. brucei* and *Leishmania* have distinct life cycles,
124 they are phylogenetically related kinetoplastid parasites that exhibit a high degree of
125 biochemical and genetic similarity (30). Indeed, the majority of orthologous genes are
126 syntenic, indicating little change in gene-order since divergence from a common ancestor.
127 Perhaps not surprisingly then, several ‘dual-purpose’ drugs display activity against both
128 parasites, including pentamidine (5), fexinidazole (11, 12) and the proteasome inhibitor,
129 GNF6702 (31). *T. brucei* is also susceptible to *in vitro* killing by the four current anti-
130 leishmanial drugs. Therefore, we hypothesised that *T. brucei* RNAi library selection in the
131 anti-leishmanial drugs would enable identification of candidate drug efficacy determinants
132 with orthologues in *Leishmania*.

133 Here, we describe RIT-seq library screening using each of the current anti-
134 leishmanial drugs. We identified 44 high confidence putative drug efficacy determinants,
135 including the *T. brucei* orthologues of the *Leishmania* SSG and miltefosine transporters.
136 Among many previously unknown drug efficacy determinants, we found that the vesicle-

137 associated membrane protein, TbVAMP7B, contributes to miltefosine and amphotericin-B
138 efficacy, and highlight a role for a cohort of amino phospholipid-transporting P4-ATPases
139 (or 'flippases') in driving amphotericin-B efficacy. This collection of validated and putative
140 anti-leishmanial drug efficacy determinants provides new insight into mode-of-action and
141 potential resistance mechanisms, and represents an important resource to guide future
142 study.

143 **Results**

144 **Orthology-based chemogenomic profiles for anti-leishmanial drugs**

145 The four current anti-leishmanial drugs, sodium stibogluconate (SSG),
146 paromomycin, miltefosine and amphotericin-B, have *in vitro* EC₅₀ values against *T. brucei*
147 of 1.8 µg.ml⁻¹, 17 µM, 30 µM and 260 nM, respectively (Fig. 1A). The equivalent values
148 versus intracellular *L. donovani* amastigotes in mouse peritoneal macrophages are
149 approximately an order of magnitude higher (SSG, paromomycin) or lower (miltefosine,
150 amphotericin-B) (32). To identify factors whose loss renders *T. brucei* less sensitive to
151 each anti-leishmanial drug, a bloodstream-form (BSF) *T. brucei* RNAi library was induced
152 for 24 hours then each drug added at 1-3X EC₅₀; selection and induction were maintained
153 thereafter (Fig. 1B). After selection for approximately 10 days, populations with reduced
154 drug sensitivity emerged and grew consistently under continued selection (Fig. 1C).

155 Following robust growth for at least two days, genomic DNA was isolated from the
156 drug-selected populations and subjected to RNAi construct-specific PCR, generating
157 distinct banding patterns for each (Fig. 1C). We sequenced the amplified RNAi target
158 fragment populations from the selected RNAi libraries on an Illumina HiSeq platform
159 (Table S1). For each selected RNAi library, we mapped more than three million individual
160 sequence reads, representing anti-leishmanial enriched RNAi target fragments, to the
161 TREU927 *T. brucei* reference genome (33) using our established RIT-seq methodology
162 (34) (Fig. 1B). The presence of the RNAi construct-specific barcode identified 'high
163 confidence' hits, i.e. those represented by more than 99 barcoded
164 reads/kilobase/predicted transcript (open reading frames plus predicted untranslated
165 regions, as annotated in the TREU927 reference genome available at www.tritrypdb.org),
166 and recovery of at least two independent RNAi target fragments (Fig. 2; Fig. S1; Table
167 S1).

168 Importantly, we identified *T. brucei* orthologues of two known *Leishmania*
169 determinants of anti-leishmanial drug efficacy. RNAi target fragments that mapped to the
170 *TbAQP2-3* locus (Tb927.10.14160-70), which encodes two aquaglyceroporins, dominated
171 the SSG-selected RNAi library; *L. donovani* AQP1 (LdBPK_310030.1) is a key mediator of
172 SSG uptake (19). Another significant hit identified following miltefosine selection was a
173 putative flippase (Tb927.11.3350); the corresponding coding sequence is syntenic with the
174 *L. donovani* miltefosine transporter (LdBPK_131590.1) (17). The identification of *T. brucei*
175 orthologues of these known anti-leishmanial efficacy determinants highlights the power of
176 this chemogenomic profiling approach in the identification of mechanisms of action and
177 resistance that are also relevant to *Leishmania* parasites. In addition to these hits, our RIT-
178 seq analyses yielded a further 42 high confidence hits (Fig. 2; Fig. S1; Table S1).

179

180 **TbAQP3, an orthologue of *Leishmania* AQP1, is linked to antimonial action.**

181 Aquaglyceroporin defects in *T. brucei* and in *Leishmania* have been linked to
182 arsenical and antimonial resistance (see above), but specific relationships among drugs
183 and AQPs have not been fully elucidated. For example, TbAQP2 is responsible for
184 pentamidine and melarsoprol uptake (35), possibly *via* receptor-mediated endocytosis in
185 the former case (36), and mutations that disrupt *TbAQP2* are responsible for melarsoprol
186 resistance in patients (37). *L. donovani* AQP1 has also been linked to antimonial
187 resistance in patients (38). Notably, TbAQP3 and *Leishmania* AQP1 have the same set of
188 selectivity filter residues (NPA/NPA/WGYR), while TbAQP2 has a divergent set
189 (NSA/NPS/IVLL) (39). Therefore, we investigated the specificity of the interaction between
190 SSG and TbAQP2/TbAQP3, the major hits in the SSG screen.

191 Sequence mapping of the RNAi target fragments following SSG selection revealed
192 that approximately 71% and 29% of mapped reads containing the RNAi construct-specific
193 barcode corresponded to *TbAQP2* (Tb927.10.14170) and *TbAQP3* (Tb927.10.14160),

194 respectively (Fig. 3A); only 0.08% of reads mapped elsewhere in the genome. These data
195 are consistent with the idea that both aquaglyceroporins contribute to SSG action.
196 However, the *TbAQP2* and *TbAQP3* coding sequences are 82.3% identical, thus while an
197 RNAi fragment may unambiguously map to *TbAQP2*, it may be sufficiently similar to
198 *TbAQP3* to elicit its depletion. Therefore, we tested the relative contribution of the encoded
199 aquaglyceroporins to SSG action against *T. brucei* using *aqp2-3* null and re-expression
200 cell lines (35).

201 Deletion of the *TbAQP2-3* locus led to a 6.7-fold increase in SSG EC₅₀ (Fig. 3B),
202 consistent with the output from the screen. Inducible expression of ^{GFP}TbAQP2 in the null
203 cell line had little effect on *T. brucei* SSG sensitivity (Fig. 3C, left-hand panel); however,
204 ^{GFP}TbAQP3 expression reduced the SSG EC₅₀ 5.5-fold (Fig. 3C, right-hand panel). In
205 contrast, and as shown previously (35), ^{GFP}AQP2 expression complemented the
206 pentamidine resistance of *aqp2-3* null *T. brucei* (Fig. 3D, left-hand panel), while ^{GFP}AQP3
207 expression had no effect on pentamidine sensitivity (Fig. 3C, right-hand panel). Therefore,
208 SSG sensitivity and resistance is specifically determined by TbAQP3 expression. This
209 indicates that the NPA/NPA/WGYR selectivity filter, present in both TbAQP3 (39) and
210 *Leishmania* AQP1, may be selective for antimonial uptake.

211

212 ***T. brucei* lysosomal MFST influences aminoglycoside action.**

213 Selection of the BSF *T. brucei* RNAi library with the anti-leishmanial
214 aminoglycoside, paromomycin, identified 50 hits, of which 28 fulfilled our high stringency
215 criteria (Table S1). Twenty-one of the high confidence hits were functionally annotated,
216 and included several associated with transport and nucleic acid processing. The top three
217 hits with functional annotations were *Tb927.9.6360-80* (major facilitator superfamily
218 transporters, MFST), *Tb927.11.6680* (amino acid transporter, AAT15) and
219 *Tb927.11.14190* (Tudor domain-containing Staphylococcal nuclease, TSN) (40), targeted

220 by approximately 84%, 1.7% and 0.9% of the mapped reads, respectively (Fig. 4A, Fig. S2
221 and Table S1). However, while parasites able to deplete AAT15 and TSN persisted in the
222 population over the 12 days of selection in paromomycin, we were unable to detect a
223 significant advantage versus wild type *T. brucei* during the course of a standard 72-hour
224 EC₅₀ assay (Fig. S1). Therefore, we focussed our attention on the MFST genes.

225 The genes at the *Tb927.9.6360-80* locus share at least 92% sequence identity and
226 encode for three putative MFSTs, a ubiquitous family of proteins responsible for
227 membrane transit of a wide range of solutes including drugs (41). Comparison with the
228 sequences annotated 'MFS' or 'major facilitator superfamily transporter' in the *L. major*
229 reference genome confirmed that the syntenic coding sequence, *LmjF.15.0870*, is most
230 closely related to *Tb927.9.6360-80* (Fig. 4B; Fig. S3). The *Leishmania* and *T. brucei*
231 proteins share a similar *trans*-membrane domain organisation and the cytoplasmic loop
232 between TM6 and TM7, which is characteristic of MFST proteins (Fig. 4C) (42).

233 We previously identified the *Tb927.9.6360-80* locus as a key contributor to suramin
234 efficacy against *T. brucei*, with RNAi depletion of the three transcripts leading to a ten-fold
235 reduction in parasite sensitivity to suramin; localisation studies also indicated that at least
236 one of these transporters is lysosomal (24). Deletion of the whole locus (Fig. 4D) revealed
237 that the three encoded proteins are collectively dispensable in cultured BSF *T. brucei* (Fig.
238 4E), and enabled us to confirm that not only do these proteins influence suramin efficacy
239 (Fig. 4F), but also that of paromomycin (Fig. 4G) and the related aminoglycoside,
240 neomycin (Fig. 4H). While loss of these MFST proteins dramatically reduces suramin
241 efficacy, the effect on paromomycin and neomycin sensitivity is less pronounced (1.5 and
242 2.8-fold EC₅₀ increase, respectively), though significant. Our mutant BSF *T. brucei* also
243 exhibited better tolerance than wild type parasites to the aminoglycosides at
244 concentrations equivalent to greater than EC₉₉ during the first 24 hours of exposure (Fig.
245 S4).

246

247 **TbVAMP7B, a cross-efficacy determinant for amphotericin-B and miltefosine.**

248 To identify anti-leishmanial cross-efficacy determinants, we next used pairwise
249 comparisons of RNAi library screen outputs (Fig. 5). We first identified a small cohort of
250 hits represented by at least two RNAi target fragments and >99 reads/kilobase/transcript in
251 more than one screen. This group included the *AQP2-3* locus, represented by at least 100
252 reads in all four screens. We did not explore this locus further since the read-count was at
253 least three orders of magnitude lower in each screen relative to the SSG screen, and
254 leishmanial AQPs have not been implicated in resistance to the other drugs (see above).
255 Two other loci fulfilled our stringency criteria, and both were enriched following
256 amphotericin-B and miltefosine selection: *Tb927.5.3550-70* and *Tb927.11.3350* (Table
257 S1); further analysis of the former hit is considered in this section, while the contribution of
258 *Tb927.11.3350* to drug action is addressed subsequently.

259 RIT-seq analysis revealed that 2.2% and 97% of mapped reads identified
260 *Tb927.5.3550-70* in the amphotericin-B and miltefosine screens, respectively (Fig. 6A).
261 This locus encodes for a thioredoxin-like protein (*Tb927.5.3550*), a vesicle-associated
262 membrane protein, TbVAMP7B (*Tb927.5.3560*) (43), and a hypothetical protein
263 (*Tb927.5.3570*). Analysis of the RNAi target fragments mapping to *Tb927.5.3550-70*
264 revealed that few uniquely targeted the *TbVAMP7B* coding sequence (Fig. 6A). Instead,
265 the RNAi target fragments that mapped to the flanking genes overlapped either the
266 *TbVAMP7B* coding sequence (3550 RNAi target fragments) or 3'-untranslated region
267 (3570 RNAi target fragments). This pattern is consistent with poor tolerance of TbVAMP7B
268 depletion. Our previous high-throughput phenotypic analysis indicated that TbVAMP7B
269 RNAi knockdown is associated with a significant loss of fitness, while depletion of the
270 flanking transcripts had a less dramatic effect (Table S1) (44). Taken together, these data

271 suggested that TbVAMP7B is an amphotericin-B/miltefosine cross-efficacy determinant,
272 while the identification of the flanking genes was due to bystander effects.

273 To test this hypothesis, we generated stem-loop RNAi BSF *T. brucei* cell lines
274 targeting TbVAMP7B and Tb927.5.3570. As predicted, depletion of Tb927.5.3570 had no
275 effect on growth or sensitivity to amphotericin-B or miltefosine (Fig. S5). In contrast,
276 knockdown of TbVAMP7B following induction in tetracycline at 2 ng or 1 $\mu\text{g.ml}^{-1}$ resulted in
277 a significant growth defect (Fig. 6B). To assess the contribution of TbVAMP7B to drug
278 efficacy, we induced RNAi in 2 ng.ml⁻¹ tetracycline for 24 hours and assessed drug
279 sensitivity over a further 30 hours under inducing conditions. Incubation in low
280 concentration tetracycline and a shorter EC₅₀ analysis (as opposed to the standard 72-
281 hour protocol) ensured that the growth defect due to TbVAMP7B RNAi knockdown was
282 minimised, while still allowing us to test the protein's contribution to drug action.

283 Unexpectedly, RNAi knockdown of TbVAMP7B reduced the amphotericin-B EC₅₀,
284 by 24% (Fig. 6C). However, TbVAMP7B depletion also resulted in a significant decrease
285 in the Hill coefficient. Consequently, while the EC₅₀ decreased upon TbVAMP7B depletion,
286 the EC₉₀ and EC₉₉ increased 1.45-fold and 3-fold, respectively (Fig. 6D); the EC₂₅
287 decreased by 44%, consistent with the effect on the EC₅₀ and the change in the Hill
288 coefficient. Therefore, small changes in TbVAMP7B expression can lead to significant loss
289 of sensitivity to high concentration amphotericin-B, while enhancing sensitivity to the drug
290 at low concentration. This relative resistance to high concentration amphotericin-B
291 explains the enrichment of TbVAMP7B-targeting RNAi fragments following selection of the
292 RNAi library in 1.5x EC₅₀. In contrast, miltefosine at relatively low concentrations
293 complemented the TbVAMP7B RNAi growth defect and further increased growth at lower
294 concentrations (Fig. 6E, F).

295 Our findings indicate specific interactions between TbVAMP7B and both
296 amphotericin-B and miltefosine. VAMP7 proteins are involved in endosome and lysosome

297 membrane fusion (45) and it is notable in this respect that amphotericin-B disrupts
298 membranes and miltefosine is a phospholipid drug. TbVAMP7B depletion does not
299 significantly increase the EC₅₀ for either drug but, nevertheless, these interactions may be
300 important in a clinical setting where exposure will be variable in different tissues and at
301 different times following dosing.

302

303 **Multiple hits link amphotericin-B action to phospholipid transport and metabolism.**

304 Our amphotericin-B screen yielded thirteen high-confidence hits, for which Gene-
305 Ontology term profiling revealed links to membranes and lipids (Table S2; Fig. S6). This is
306 consistent with disruption of membranes by amphotericin-B. Miltefosine uptake in
307 *Leishmania* is dependent on a flippase (17, 18), which also contributes to the anti-
308 leishmanial action of amphotericin-B (46). RNAi fragments targeting the syntenic locus in
309 *T. brucei*, Tb927.11.3350, were enriched following selection in amphotericin-B and
310 miltefosine (Fig. 5; Fig. 7A). Depletion of Tb927.11.3350, while having no effect on
311 parasite growth in culture (Fig. 7B), led to a reproducible increase in amphotericin-B and
312 miltefosine EC₅₀ (Fig. 7C, D). RNAi knockdown also significantly enhanced short-term
313 survival in high concentration amphotericin-B and miltefosine (Fig. S6). Therefore, as in
314 *Leishmania*, the *T. brucei* miltefosine transporter orthologue contributes to the action of
315 miltefosine and amphotericin-B.

316 In addition to Tb927.11.3350, the *T. brucei* genome contains three other putative
317 flippases (Fig. 8A), as well as three putative β-subunits, including Tb927.11.13770, the
318 syntenic orthologue of *Leishmania* Ros3 (18). Three of the four flippases (Tb927.4.1510,
319 Tb927.11.3350 and Tb927.11.13000) have a similar domain organisation to the yeast
320 flippases and possess the DEGT and DKTGT motifs characteristic of the actuator and
321 phosphorylation domains (47). The fourth, Tb927.6.3550, lacks the flippase DEGT domain,
322 although it clusters with the *Leishmania* flippase, LmjF.34.2630. However, it also lacks the

323 TGES domain characteristic of the related cation transporting P-type ATPases, such as
324 yeast Pay2 (47), so its identity is unclear (Fig. 8A).

325 In addition to the *Leishmania* miltefosine transporter orthologue, Tb927.11.3350,
326 RNAi fragments targeting the flippases, Tb927.11.13000 and Tb927.6.3550, and the β -
327 subunit, Tb927.11.13200, were enriched following selection in amphotericin-B, with
328 Tb927.11.13000 represented by 78% of mapped reads (Fig. 8B; Table S1). Targeted RNAi
329 depletion of Tb927.11.13000 led to a mild growth defect (Fig. 8C) and a more than two-
330 fold EC₅₀ increase, validating this protein as an amphotericin-B efficacy determinant in *T.*
331 *brucei* (Fig. 8D). The impact of Tb927.11.13000 depletion was most pronounced during
332 the initial 24 hours of drug exposure, enabling the parasite population to increase
333 approximately 1.3-fold and four-fold over eight and 24 hours, respectively, in the presence
334 of 0.7 μ M (>EC₉₉) amphotericin-B (Fig. S6). The uninduced population declined by more
335 than 40% and 60% over the same periods. In addition, while exposure to 1.8 μ M (>EC_{99.9})
336 amphotericin-B led to an 80% decline in the induced population over 24 hours, cultures of
337 uninduced cells were cleared within four hours exposure to this drug concentration (Fig.
338 S6). Depletion of this putative phospholipid-transporting ATPase had no effect on
339 miltefosine efficacy (Fig. 8E) confirming its specific contribution to amphotericin-B action.

340 Our results reveal that multiple *T. brucei* flippases drive the efficacy of
341 amphotericin-B, all of which have syntenic orthologues in *Leishmania* (Fig. 8A). Therefore,
342 in addition to the well-characterised miltefosine-transporting flippase, other *Leishmania*
343 flippases may play significant, and potentially specific, roles in the anti-leishmanial action
344 of amphotericin-B and miltefosine.

345

346 Discussion

347 In the current absence of an effective genome-scale loss-of-function screen in
348 *Leishmania*, we speculated that selection of a *T. brucei* RNAi library would provide insights

349 into anti-leishmanial drug action, while also revealing novel *T. brucei* biology. By selecting
350 our genome-scale BSF *T. brucei* RNAi library in the current anti-leishmanial drugs followed
351 by RIT-seq analysis, we identified a panel of putative anti-leishmanial drug efficacy
352 determinants (Table S1 and Fig. S1). SSG and miltefosine selection respectively identified
353 TbAQP3, an orthologue of the known SSG transporter, and Tb927.11.3350, the *T. brucei*
354 orthologue of the *Leishmania* miltefosine transporter, confirming the power of this
355 approach. In addition to these known drug transporters, we validated several novel drug
356 efficacy determinants identified by our selective screens: Tb927.9.6360-80 (paromomycin),
357 Tb927.5.3560 (miltefosine and amphotericin-B) and Tb927.11.13000 (amphotericin-B).
358 Our results highlight the role of a lysosomal transporter in paromomycin efficacy,
359 emphasise the importance of membrane composition in the action of amphotericin-B and
360 miltefosine, provide insight into the substrate selectivity of the trypanosomatid
361 aquaglyceroporins, and present several new candidate anti-leishmanial drug efficacy
362 determinants (Fig. 9).

363 *T. brucei* RNAi library selection in SSG and our subsequent validation experiments
364 identified a single efficacy determinant, TbAQP3. Aquaglyceroporins are ubiquitous
365 transporters of water, glycerol and other small solutes, whose specificity is defined by their
366 selectivity filter residues. *Leishmania* AQP1 and the *T. brucei* proteins, TbAQP1 and
367 TbAQP3, have the same selectivity filter, NPA/NPA/WGYR, while TbAQP2 possesses a
368 divergent filter, NSA/NPS/IVLL (39). TbAQP2 is a key drug transporter in *T. brucei*,
369 mediating the uptake of pentamidine and melarsoprol, and its loss contributes to clinical
370 drug resistance (35-37). In addition, TbAQP2 plays an important role in glycerol transport,
371 as its loss increases parasite sensitivity to alternative oxidase inhibition, which leads to
372 elevated intracellular glycerol levels (48). The *in vivo* roles of the other *T. brucei*
373 aquaglyceroporins remain unknown, though all three are capable of arsenite and
374 antimonite transport in yeast and *Xenopus* heterologous expression systems (49). In

375 contrast, our data demonstrate that in *T. brucei* these transporters are selective for
376 arsenic-containing melarsoprol (TbAQP2; (35)) and antimony-containing, SSG (TbAQP3).
377 Intriguingly, RNAi library selection with SSG failed to identify TbAQP1 even though it
378 contains the same selectivity filter as TbAQP3. This suggests important functional and
379 regulatory differences between TbAQP1 and TbAQP3, which may influence their ability to
380 contribute to SSG uptake in bloodstream-form *T. brucei*. For example, TbAQP3 is
381 localised to the plasma membrane in bloodstream-form *T. brucei* and TbAQP1 localises to
382 the flagella membrane (35, 50). This differential localisation may influence their ability to
383 mediate antimonial uptake.

384 The aminoglycoside, paromomycin, is thought to inhibit protein synthesis in
385 *Leishmania* and enters the cell *via* endocytosis (21, 51, 52). However, RNAi library
386 selection did not identify a surface receptor suggesting that, at least in *T. brucei*,
387 paromomycin entry is not dependent on a specific ligand-receptor interaction. Rather, the
388 high endocytic flux associated with surface VSG internalisation (53) may drive drug
389 uptake. RNAi fragments targeting Tb927.9.6360-80 dominated the paromomycin-selected
390 RNAi library, with the remaining 28 high confidence hits constituting only 9% of mapped
391 reads. This locus encodes a set of closely related MFST proteins, at least one of which
392 localises to the lysosome, and has previously been associated with suramin efficacy (24).
393 In contrast to paromomycin, several other endocytic pathway proteins, including three
394 lysosomal proteins (p67, cathepsin-L and the MFST proteins), influence suramin efficacy
395 (24). This led to the proposal that proteolytic processing in the lysosome releases suramin
396 from bound proteins, enabling neutralisation in the acidic environment or association with
397 an alternative endogenous carrier and escape to the cytoplasm *via* one or more of the
398 lysosomal MFSTs (54). In contrast, the absence of hits targeting other endocytic
399 components following paromomycin RNAi library selection suggests little reliance on the
400 endocytic network *per se*. Therefore, the lysosomal MFST proteins may influence

401 paromomycin efficacy indirectly. MFST proteins mediate the transit of a diverse range of
402 molecules, including polyamines and amino acids (41), and changes in the intracellular
403 flux of these molecules may affect translation efficiency, which in turn may influence
404 paromomycin efficacy. Deletion of the *Tb927.9.6360-80* locus from *T. brucei* yields only a
405 two-fold increase in paromomycin EC₅₀. However, the MFST protein encoded by the
406 syntenic single copy gene in *Leishmania* (e.g. *LmjF.15.0870*) remains to be characterised
407 and may make a more substantial contribution to paromomycin action against this
408 parasite.

409 Combination therapies are increasingly being used to treat leishmaniasis, enabling
410 reduced dosing and treatment duration, resulting in fewer side effects (8). For example, a
411 single dose of liposomal amphotericin-B in combination with a short course of oral
412 miltefosine or intramuscular paromomycin is an effective treatment for visceral
413 leishmaniasis (VL) in the Indian sub-continent (55). In East Africa, SSG-paromomycin
414 combination therapy is effective against VL (56). However, *L. donovani* resistant to these
415 and other anti-leishmanial drug combinations can be selected for *in vitro* (9, 10), and
416 oxidative defence upregulation and changes in membrane fluidity have been associated
417 with cross-resistance in laboratory-derived lines (23). Therefore, we carried out pairwise
418 comparisons of our RNAi library screen data to identify potential cross-efficacy
419 determinants. Only two hits fulfilled our stringency criteria, both of which influence
420 amphotericin-B and miltefosine action: TbVAMP7B, an endosomal SNARE protein
421 responsible for endosomal-lysosomal fusion in other eukaryotes (45, 57), and
422 Tb927.11.3350, the *T. brucei* orthologue of the *Leishmania* miltefosine transporter (17).
423 However, while both of these proteins may influence membrane fluidity (see below), it
424 seems unlikely that either contributes significantly to oxidative defence. Recent Cos-seq
425 gain-of-function analyses in *L. infantum* identified several candidate proteins whose
426 overexpression reduces sensitivity to multi-drug exposure (26); these also lack an obvious

427 connection to oxidative defence. Therefore, rather than being dependent on the increase
428 or decrease in expression of a single protein, changes in oxidative defence that lead to
429 anti-leishmanial resistance are likely to be multi-factorial. Our findings also suggest that
430 miltefosine/amphotericin-B combination therapy is the most vulnerable to loss-of-function
431 mutation, while others may be less susceptible to the down-regulation of a single protein.
432 This finding is particularly significant, given that recent trials have confirmed the efficacy of
433 amphotericin-B/miltefosine combination therapy in treating VL (58, 59).

434 In contrast to the other anti-leishmanial drug efficacy determinants described
435 herein, TbVAMP7B depletion does not simply increase the drugs' EC₅₀. Instead,
436 TbVAMP7B RNAi knockdown reduces amphotericin-B EC₅₀ and has little effect on
437 miltefosine EC₅₀. The drop in amphotericin-B EC₅₀ is due to a substantial decrease in the
438 amphotericin-B Hill coefficient, which has the opposite effect on EC₉₀ and EC₉₉, increasing
439 both and enabling TbVAMP7B-depleted parasites to persist at these drug concentrations.
440 Our data shows that *T. brucei* has limited tolerance for TbVAMP7B depletion, presumably
441 due to impairment of endosomal-lysosomal fusion (45). Intriguingly, exposure to low
442 concentration miltefosine complements the growth defect seen following TbVAMP7B
443 depletion, suggesting that miltefosine treatment is able to promote vesicle membrane
444 fusion in the endocytic system, a possible consequence of the enhanced membrane
445 fluidity seen upon miltefosine exposure (60). TbVAMP7B has also recently been identified
446 as a putative *T. brucei* apolipoprotein-L1 sensitivity determinant (61), and other workers
447 have highlighted the importance of the intracellular transit of apoL1-carrying membrane to
448 trypanolysis (62, 63). Our findings suggest that such transit also contributes to
449 amphotericin-B and miltefosine action. The VAMP7 proteins are highly conserved between
450 *T. brucei* and *Leishmania* (43), suggesting that *Leishmania* parasites will also be sensitive
451 to VAMP7B loss (LmjF.08.0030). However, subtle changes in VAMP7B expression that

452 can be tolerated may enable parasites to take advantage of variations in amphotericin-B
453 and miltefosine tissue penetrance.

454 Miltefosine uptake in *Leishmania* is dependent on a phospholipid-transporting
455 flippase (the miltefosine transporter, MT) and its β -subunit, Ros3 (17, 18); both *in vitro*
456 selected lines and miltefosine resistant *L. donovani* clinical isolates harbour mutations in
457 the MT (7, 64, 65). Consistent with this, *T. brucei* RNAi library selection in miltefosine led
458 to enrichment for RNAi fragments mapping to the syntenic sequence in *T. brucei*
459 (*Tb927.11.3350*). RNAi library selection in amphotericin-B also enriched for RNAi
460 fragments mapping to this gene, consistent with recent findings in *Leishmania* (46), as well
461 as two other flippases and a putative β -subunit (*Tb927.11.13200*). Interestingly, the β -
462 subunit targeted was not the syntenic orthologue of Ros3, previously shown to interact
463 with the MT (18). Therefore, different flippase/ β -subunit dependencies may have evolved
464 following divergence of the *Leishmania* and *T. brucei* lineages. A further difference in the
465 behaviour of these proteins between *Leishmania* and *T. brucei* lies in their localisation.
466 The MT and Ros3 localise to the plasma membrane in *Leishmania* (18), whereas the *T.*
467 *brucei* MT orthologue (*Tb927.11.3350*) and a second flippase (*Tb927.11.13000*) localise to
468 an intracellular structure reminiscent of the endosomal system in procyclic form *T. brucei*
469 (www.TrypTag.org; (66)). Therefore, while flippases influence drug action against
470 *Leishmania* and *T. brucei*, they may mediate drug and/or phospholipid transit across
471 different membranes in each parasite.

472 Phospholipid transport by flippases maintains the membrane asymmetry necessary
473 for membrane fusion, vesicle trafficking and sterol homeostasis (47). The identification of a
474 single flippase following miltefosine selection is consistent with its role as a drug
475 transporter (17). In contrast, amphotericin-B selection identified three flippases, suggesting
476 an indirect role in drug action, possibly through changes in membrane composition and
477 transit through the endosomal system (Fig. 9). Amphotericin-B acts by binding membrane

478 ergosterol (67), leading to the formation of ion-permeable channels and downstream
479 oxidative damage (68). Consistent with the importance of ergosterol to amphotericin-B
480 action, resistant clinical isolates exhibit elevated membrane fluidity and reduced ergosterol
481 content (69). Recent findings have highlighted the loss of key sterol biosynthetic enzymes,
482 and reduced ergosterol production, as a driver of resistance in laboratory-derived
483 amphotericin-B resistant *L. mexicana* (70). Changes in flippase expression may similarly
484 affect ergosterol membrane content and/or accessibility, thereby reducing sensitivity to
485 amphotericin-B. Therefore, functional characterisation of the syntenic orthologues of these
486 proteins in *Leishmania* may provide further insights into the processes and factors that
487 drive the anti-leishmanial action of amphotericin-B.

488 In summary, using our genome-scale BSF *T. brucei* RNAi library we have identified
489 a panel of putative anti-leishmanial drug efficacy determinants, highlighting two candidate
490 cross-efficacy determinants, as well as roles for multiple flippases in the action of
491 amphotericin-B. The findings from this orthology-based chemogenomic profiling approach
492 substantially advance our understanding of anti-leishmanial drug mode-of-action and
493 potential resistance mechanisms, and should facilitate the development of improved
494 therapies, as well as surveillance for drug-resistant parasites.

495 **Methods**

496 ***T. brucei* strains**

497 MITat1.2/2T1 BSF *T. brucei* (71) were maintained in HMI11 (Invitrogen, LifeTech)
498 supplemented with 10% foetal calf serum (Sigma) at 37°C/5% CO₂. Transfection was
499 carried out in either cytomix or Tb-BSF buffer (72), for integration at the 2T1 'landing pad'
500 (71, 73) or *Tb927.9.6360-80*, respectively, using a Nucleofector (Lonza) set to programme
501 X-001. Transformants were selected in 2.5 µg.ml⁻¹ hygromycin, 2 µg.ml⁻¹ puromycin or 10
502 µg.ml⁻¹ blasticidin, as appropriate. The BSF *T. brucei* RNAi library was maintained in 1
503 µg.ml⁻¹ phleomycin and 5 µg.ml⁻¹ blasticidin (34). For growth assays, cultured BSF *T.*
504 *brucei* were seeded at ~10⁵ cells.ml⁻¹, counted using a haemocytometer, and diluted back
505 every 24 hours, as necessary, for three days in the absence of antibiotics. All selective
506 antibiotics were purchased from Invivogen.

507

508 **Drug sensitivity assays**

509 Half-maximal effective concentrations (EC₅₀) of the anti-leishmanial drugs (sodium
510 stibogluconate, GSK; paromomycin, Sigma; miltefosine, Paladin; amphotericin-B, E R
511 Squibb, UK) and neomycin (G418, Invivogen) were determined over 78 or 30 hours. BSF
512 *T. brucei* were seeded at 2x10³ (or 2x10⁵) cells.ml⁻¹ in 96-well plates in a 2-fold dilution
513 series of each drug; assays were carried out in the absence of other antibiotics. After 72 or
514 24 hours, resazurin (Sigma) in PBS was added to a final concentration of 12.5 µg.ml⁻¹ per
515 well, and the plates incubated for a further 6 hours at 37°C. Fluorescence was determined
516 using a fluorescence plate reader (Molecular Devices) at an excitation wavelength of 530
517 nm, an emission wavelength of 585 nm and a filter cut-off of 570 nm (74). Data were
518 processed in Microsoft Excel, and non-linear regression analysis carried out in GraphPad
519 Prism. The short-term kinetics of killing in high concentration drug (>EC₉₉) were
520 determined in triplicate over 24 hours from a starting cell density of 1x10⁵ cells.ml⁻¹.

521

522 ***T. brucei* RNAi library screening and RIT-seq**

523 RNA library screening was carried out as previously described (34). Briefly, library
524 expression was induced in $1 \mu\text{g}\cdot\text{ml}^{-1}$ tetracycline (Sigma) for 24 hours prior to selection in
525 each anti-leishmanial drug at 1-3X EC_{50} . Cell density was assessed daily using a
526 haemocytometer and diluted to no less than 20 million cells in 100 ml media; induction and
527 anti-leishmanial drug selection were maintained throughout. Once robust growth had been
528 achieved for at least two days, genomic DNA was prepared for RNAi target identification.
529 The RNAi cassettes remaining in the anti-leishmanial-selected RNAi libraries were
530 amplified from genomic DNA using the LIB2F/LIB2R primers and sequenced on an
531 Illumina HiSeq platform at the Beijing Genome Institute.

532 The sequenced RNAi target fragments were mapped against the *T. brucei* strain
533 TREU927 reference genome (release 6.0), as described (34). Briefly, mapping was carried
534 out using Bowtie2 (75) set to 'very sensitive local' alignment and output SAM files were
535 processed using SAMtools (76). The resultant BAM files were viewed against the
536 reference genome in the Artemis genome browser (77). Reads containing the RNAi
537 construct-specific 14-base barcode were identified using a custom script (34), and
538 corresponded to at least 22% of reads from each selected RNAi library. This subset of
539 reads were mapped against the TREU927 reference genome, as above. Plots were
540 generated using the Artemis graph tool and processed in Adobe Photoshop Elements 8.0.
541 Stacks of reads that included the 14-base barcode on the positive strand were used to
542 define RNAi target fragment junctions and to assign high-confidence hits as those
543 identified by at least two RNAi target fragments. RNAi target fragment read numbers were
544 converted to RPKM (reads/kilobase/million reads mapped) to account for inter-library read-
545 depth variations when comparing RNAi library sequencing outputs.

546 Alignments were carried out in Clustal Omega
547 (<https://www.ebi.ac.uk/Tools/msa/clustalo/>), unrooted neighbour joining trees were
548 formatted in Dendroscope 3 (<http://dendroscope.org/>) (78) and putative *trans*-membrane
549 domains identified using TOPCONS (<http://topcons.cbr.su.se/>) (79). GO-term profiles were
550 constructed using the GO analysis tool at <http://tritypdb.org>.

551

552 **Plasmid and *T. brucei* strain construction and analysis**

553 *Tb927.9.6360-80* locus targeting fragments were cloned into pPAC and pBSD,
554 enabling replacement of both alleles of the three-gene locus with puromycin
555 acetyltransferase (*PAC*) and blasticidin-S deaminase (*BSD*) open reading frames. Stem-
556 loop RNAi constructs targeting *Tb927.11.6680* (*AAT15*), *Tb927.11.13000*, *Tb927.11.3350*,
557 *Tb927.5.3560* (*TbVAMP7B*) and *Tb927.5.3570* were assembled in pRPa-iSL (73). RNAi
558 targeting fragments were designed using the RNAit primer design algorithm to minimise
559 off-target effects (80). pRPa-iSL constructs were linearised with *Ascl* (NEB) prior to
560 transfection and targeted integration at the *rDNA* spacer 'landing pad' locus in 2T1 BSF *T.*
561 *brucei* (71). Details of all primers are available upon request. *Tb927.9.6360-80* allelic
562 replacement was confirmed by Southern hybridisation following *XhoI* (New England
563 Biolabs) digestion of genomic DNA. RNAi knockdown was confirmed by northern
564 hybridisation of total RNA or, in the case of *Tb927.11.6680*, by RT-qPCR, as described
565 (81). For Southern and northern hybridisation, digoxigenin-dUTP (Roche) labelled DNA
566 probes were generated by PCR, hybridised and detected according to standard protocols
567 and the manufacturer's instructions.

568

569 **Data availability**

570 Sequence data are available as fastq files at the European Nucleotide Archive
571 (<https://www.ebi.ac.uk/ena>) under study accession number, PRJEB31973 (amphotericin-B,

572 ERS3348616; miltefosine, ERS3348617; paromomycin, ERS3348618; sodium
573 stibogluconate, ERS3348619).

574 References

- 575 1. Torres-Guerrero E, Quintanilla-Cedillo MR, Ruiz-Esmenjaud J, Arenas R. 2017.
576 Leishmaniasis: a review. *F1000Res* 6:750.
- 577 2. Buscher P, Cecchi G, Jamonneau V, Priotto G. 2017. Human African trypanosomiasis.
578 *Lancet* 390:2397-2409.
- 579 3. Perez-Molina JA, Molina I. 2018. Chagas disease. *Lancet* 391:82-94.
- 580 4. Steverding D. 2017. The history of leishmaniasis. *Parasit Vectors* 10:82.
- 581 5. Barrett MP, Croft SL. 2012. Management of trypanosomiasis and leishmaniasis. *Br Med*
582 *Bull* 104:175-96.
- 583 6. Mandal S, Maharjan M, Singh S, Chatterjee M, Madhubala R. 2010. Assessing
584 aquaglyceroporin gene status and expression profile in antimony-susceptible and -resistant
585 clinical isolates of *Leishmania donovani* from India. *J Antimicrob Chemother* 65:496-507.
- 586 7. Srivastava S, Mishra J, Gupta AK, Singh A, Shankar P, Singh S. 2017. Laboratory
587 confirmed miltefosine resistant cases of visceral leishmaniasis from India. *Parasit Vectors*
588 10:49.
- 589 8. Ponte-Sucre A, Gamarro F, Dujardin JC, Barrett MP, Lopez-Velez R, Garcia-Hernandez R,
590 Pountain AW, Mwenechanya R, Papadopoulou B. 2017. Drug resistance and treatment
591 failure in leishmaniasis: A 21st century challenge. *PLoS Negl Trop Dis* 11:e0006052.
- 592 9. Garcia-Hernandez R, Manzano JI, Castanys S, Gamarro F. 2012. *Leishmania donovani*
593 develops resistance to drug combinations. *PLoS Negl Trop Dis* 6:e1974.
- 594 10. Hendrickx S, Inocencio da Luz RA, Bhandari V, Kuypers K, Shaw CD, Lonchamp J, Salotra
595 P, Carter K, Sundar S, Rijal S, Dujardin JC, Cos P, Maes L. 2012. Experimental induction
596 of paromomycin resistance in antimony-resistant strains of *L. donovani*: outcome
597 dependent on in vitro selection protocol. *PLoS Negl Trop Dis* 6:e1664.
- 598 11. Mesu V, Kalonji WM, Bardonneau C, Mordt OV, Blesson S, Simon F, Delhomme S,
599 Bernhard S, Kuziena W, Lubaki JF, Vuvu SL, Ngima PN, Mbembo HM, Ilunga M, Bonama
600 AK, Heradi JA, Solomo JLL, Mandula G, Badibabi LK, Dama FR, Lukula PK, Tete DN,
601 Lumbala C, Scherrer B, Strub-Wourgaft N, Tarral A. 2018. Oral fexinidazole for late-stage
602 African *Trypanosoma brucei gambiense* trypanosomiasis: a pivotal multicentre,
603 randomised, non-inferiority trial. *Lancet* 391:144-154.
- 604 12. Wyllie S, Patterson S, Stojanovski L, Simeons FR, Norval S, Kime R, Read KD, Fairlamb
605 AH. 2012. The anti-trypanosome drug fexinidazole shows potential for treating visceral
606 leishmaniasis. *Sci Transl Med* 4:119re1.
- 607 13. Deeks ED. 2019. Fexinidazole: First Global Approval. *Drugs* 79:215-220.
- 608 14. Hendrickx S, Guerin PJ, Caljon G, Croft SL, Maes L. 2018. Evaluating drug resistance in
609 visceral leishmaniasis: the challenges. *Parasitology* 145:453-463.
- 610 15. Downing T, Imamura H, Decuyper S, Clark TG, Coombs GH, Cotton JA, Hilley JD, de
611 Doncker S, Maes I, Mottram JC, Quail MA, Rijal S, Sanders M, Schonian G, Stark O,
612 Sundar S, Vanaerschot M, Hertz-Fowler C, Dujardin JC, Berriman M. 2011. Whole genome
613 sequencing of multiple *Leishmania donovani* clinical isolates provides insights into
614 population structure and mechanisms of drug resistance. *Genome Res* 21:2143-56.
- 615 16. Rastrojo A, Garcia-Hernandez R, Vargas P, Camacho E, Corvo L, Imamura H, Dujardin JC,
616 Castanys S, Aguado B, Gamarro F, Requena JM. 2018. Genomic and transcriptomic
617 alterations in *Leishmania donovani* lines experimentally resistant to antileishmanial drugs.
618 *Int J Parasitol Drugs Drug Resist* 8:246-264.
- 619 17. Perez-Victoria FJ, Gamarro F, Ouellette M, Castanys S. 2003. Functional cloning of the
620 miltefosine transporter. A novel P-type phospholipid translocase from *Leishmania* involved
621 in drug resistance. *J Biol Chem* 278:49965-71.
- 622 18. Perez-Victoria FJ, Sanchez-Canete MP, Castanys S, Gamarro F. 2006. Phospholipid
623 translocation and miltefosine potency require both *L. donovani* miltefosine transporter and
624 the new protein LdRos3 in *Leishmania* parasites. *J Biol Chem* 281:23766-75.
- 625 19. Gourbal B, Sonuc N, Bhattacharjee H, Legare D, Sundar S, Ouellette M, Rosen BP,
626 Mukhopadhyay R. 2004. Drug uptake and modulation of drug resistance in *Leishmania* by
627 an aquaglyceroporin. *J Biol Chem* 279:31010-7.
- 628 20. El Fadili K, Messier N, Leprohon P, Roy G, Guimond C, Trudel N, Saravia NG,
629 Papadopoulou B, Legare D, Ouellette M. 2005. Role of the ABC transporter MRPA (PGPA)

- 630 in antimony resistance in *Leishmania infantum* axenic and intracellular amastigotes.
631 Antimicrob Agents Chemother 49:1988-93.
- 632 21. Chawla B, Jhingran A, Panigrahi A, Stuart KD, Madhubala R. 2011. Paromomycin affects
633 translation and vesicle-mediated trafficking as revealed by proteomics of paromomycin -
634 susceptible -resistant *Leishmania donovani*. PLoS One 6:e26660.
- 635 22. Brotherton MC, Bourassa S, Legare D, Poirier GG, Droit A, Ouellette M. 2014. Quantitative
636 proteomic analysis of amphotericin B resistance in *Leishmania infantum*. Int J Parasitol
637 Drugs Drug Resist 4:126-32.
- 638 23. Berg M, Garcia-Hernandez R, Cuypers B, Vanaerschot M, Manzano JI, Poveda JA,
639 Ferragut JA, Castanys S, Dujardin JC, Gamarro F. 2015. Experimental resistance to drug
640 combinations in *Leishmania donovani*: metabolic and phenotypic adaptations. Antimicrob
641 Agents Chemother 59:2242-55.
- 642 24. Alsford S, Eckert S, Baker N, Glover L, Sanchez-Flores A, Leung KF, Turner DJ, Field MC,
643 Berriman M, Horn D. 2012. High-throughput decoding of antitrypanosomal drug efficacy
644 and resistance. Nature 482:232-6.
- 645 25. Alsford S, Kelly JM, Baker N, Horn D. 2013. Genetic dissection of drug resistance in
646 trypanosomes. Parasitology 140:1478-91.
- 647 26. Gazanion E, Fernandez-Prada C, Papadopoulou B, Leprohon P, Ouellette M. 2016. Cos-
648 Seq for high-throughput identification of drug target and resistance mechanisms in the
649 protozoan parasite *Leishmania*. Proc Natl Acad Sci U S A 113:E3012-21.
- 650 27. Corpas-Lopez V, Moniz S, Thomas M, Wall RJ, Torrie LS, Zander-Dinse D, Tinti M, Brand
651 S, Stojanovski L, Manthri S, Hallyburton I, Zuccotto F, Wyatt PG, De Rycker M, Horn D,
652 Ferguson MAJ, Clos J, Read KD, Fairlamb AH, Gilbert IH, Wyllie S. 2018. Pharmacological
653 Validation of N-Myristoyltransferase as a Drug Target in *Leishmania donovani*. ACS Infect
654 Dis doi:10.1021/acscinfecdis.8b00226.
- 655 28. Fernandez-Prada C, Sharma M, Plourde M, Bresson E, Roy G, Leprohon P, Ouellette M.
656 2018. High-throughput Cos-Seq screen with intracellular *Leishmania infantum* for the
657 discovery of novel drug-resistance mechanisms. Int J Parasitol Drugs Drug Resist 8:165-
658 173.
- 659 29. Lye LF, Owens K, Shi H, Murta SM, Vieira AC, Turco SJ, Tschudi C, Ullu E, Beverley SM.
660 2010. Retention and loss of RNA interference pathways in trypanosomatid protozoans.
661 PLoS Pathog 6:e1001161.
- 662 30. El-Sayed NM, Myler PJ, Blandin G, Berriman M, Crabtree J, Aggarwal G, Caler E, Renauld
663 H, Worthey EA, Hertz-Fowler C, Ghedin E, Peacock C, Bartholomeu DC, Haas BJ, Tran
664 AN, Wortman JR, Alsmark UC, Angiuoli S, Anupama A, Badger J, Bringaud F, Cadag E,
665 Carlton JM, Cerqueira GC, Creasy T, Delcher AL, Djikeng A, Embley TM, Hauser C, Ivens
666 AC, Kummerfeld SK, Pereira-Leal JB, Nilsson D, Peterson J, Salzberg SL, Shallom J, Silva
667 JC, Sundaram J, Westenberger S, White O, Melville SE, Donelson JE, Andersson B, Stuart
668 KD, Hall N. 2005. Comparative genomics of trypanosomatid parasitic protozoa. Science
669 309:404-9.
- 670 31. Khare S, Nagle AS, Biggart A, Lai YH, Liang F, Davis LC, Barnes SW, Mathison CJ,
671 Myburgh E, Gao MY, Gillespie JR, Liu X, Tan JL, Stinson M, Rivera IC, Ballard J, Yeh V,
672 Groessl T, Federe G, Koh HX, Venable JD, Bursulaya B, Shapiro M, Mishra PK, Spraggon
673 G, Brock A, Mottram JC, Buckner FS, Rao SP, Wen BG, Walker JR, Tuntland T, Molteni V,
674 Glynne RJ, Supek F. 2016. Proteasome inhibition for treatment of leishmaniasis, Chagas
675 disease and sleeping sickness. Nature 537:229-233.
- 676 32. Seifert K, Escobar P, Croft SL. 2010. In vitro activity of anti-leishmanial drugs against
677 *Leishmania donovani* is host cell dependent. J Antimicrob Chemother 65:508-11.
- 678 33. Berriman M, Ghedin E, Hertz-Fowler C, Blandin G, Renauld H, Bartholomeu DC, Lennard
679 NJ, Caler E, Hamlin NE, Haas B, Bohme U, Hannick L, Aslett MA, Shallom J, Marcello L,
680 Hou L, Wickstead B, Alsmark UC, Arrowsmith C, Atkin RJ, Barron AJ, Bringaud F, Brooks
681 K, Carrington M, Cherevach I, Chillingworth TJ, Churcher C, Clark LN, Corton CH, Cronin
682 A, Davies RM, Doggett J, Djikeng A, Feldblyum T, Field MC, Fraser A, Goodhead I, Hance
683 Z, Harper D, Harris BR, Hauser H, Hostetler J, Ivens A, Jagels K, Johnson D, Johnson J,
684 Jones K, Kerhornou AX, Koo H, Larke N, et al. 2005. The genome of the African
685 trypanosome *Trypanosoma brucei*. Science 309:416-22.

- 686 34. Glover L, Alsford S, Baker N, Turner DJ, Sanchez-Flores A, Hutchinson S, Hertz-Fowler C,
687 Berriman M, Horn D. 2015. Genome-scale RNAi screens for high-throughput phenotyping
688 in bloodstream-form African trypanosomes. *Nat Protoc* 10:106-33.
- 689 35. Baker N, Glover L, Munday JC, Aguinaga Andres D, Barrett MP, de Koning HP, Horn D.
690 2012. Aquaglyceroporin 2 controls susceptibility to melarsoprol and pentamidine in African
691 trypanosomes. *Proc Natl Acad Sci U S A* 109:10996-1001.
- 692 36. Song J, Baker N, Rothert M, Henke B, Jeacock L, Horn D, Beitz E. 2016. Pentamidine Is
693 Not a Permeant but a Nanomolar Inhibitor of the *Trypanosoma brucei* Aquaglyceroporin-2.
694 *PLoS Pathog* 12:e1005436.
- 695 37. Graf FE, Baker N, Munday JC, de Koning HP, Horn D, Maser P. 2015. Chimerization at the
696 AQP2-AQP3 locus is the genetic basis of melarsoprol-pentamidine cross-resistance in
697 clinical *Trypanosoma brucei gambiense* isolates. *Int J Parasitol Drugs Drug Resist* 5:65-8.
- 698 38. Imamura H, Downing T, Van den Broeck F, Sanders MJ, Rijal S, Sundar S, Mannaert A,
699 Vanaerschot M, Berg M, De Muylder G, Dumetz F, Cuypers B, Maes I, Domagalska M,
700 Decuypere S, Rai K, Uranw S, Bhattarai NR, Khanal B, Prajapati VK, Sharma S, Stark O,
701 Schonian G, De Koning HP, Settimo L, Vanhollebeke B, Roy S, Ostyn B, Boelaert M, Maes
702 L, Berriman M, Dujardin JC, Cotton JA. 2016. Evolutionary genomics of epidemic visceral
703 leishmaniasis in the Indian subcontinent. *Elife* 5.
- 704 39. Baker N, de Koning HP, Maser P, Horn D. 2013. Drug resistance in African
705 trypanosomiasis: the melarsoprol and pentamidine story. *Trends Parasitol* 29:110-8.
- 706 40. Alsford S, Kemp LE, Kawahara T, Horn D. 2010. RNA interference, growth and
707 differentiation appear normal in African trypanosomes lacking Tudor staphylococcal
708 nuclease. *Mol Biochem Parasitol* 174:70-3.
- 709 41. Dos Santos SC, Teixeira MC, Dias PJ, Sa-Correia I. 2014. MFS transporters required for
710 multidrug/multixenobiotic (MD/MX) resistance in the model yeast: understanding their
711 physiological function through post-genomic approaches. *Front Physiol* 5:180.
- 712 42. Yan N. 2015. Structural Biology of the Major Facilitator Superfamily Transporters. *Annu*
713 *Rev Biophys* 44:257-83.
- 714 43. Murungi E, Barlow LD, Venkatesh D, Adung'a VO, Dacks JB, Field MC, Christoffels A.
715 2014. A comparative analysis of trypanosomatid SNARE proteins. *Parasitol Int* 63:341-8.
- 716 44. Alsford S, Turner DJ, Obado SO, Sanchez-Flores A, Glover L, Berriman M, Hertz-Fowler C,
717 Horn D. 2011. High-throughput phenotyping using parallel sequencing of RNA interference
718 targets in the African trypanosome. *Genome Res* 21:915-24.
- 719 45. Ward DM, Pevsner J, Scullion MA, Vaughn M, Kaplan J. 2000. Syntaxin 7 and VAMP-7 are
720 soluble N-ethylmaleimide-sensitive factor attachment protein receptors required for late
721 endosome-lysosome and homotypic lysosome fusion in alveolar macrophages. *Mol Biol*
722 *Cell* 11:2327-33.
- 723 46. Fernandez-Prada C, Vincent IM, Brotherton MC, Roberts M, Roy G, Rivas L, Leprohon P,
724 Smith TK, Ouellette M. 2016. Different Mutations in a P-type ATPase Transporter in
725 *Leishmania* Parasites are Associated with Cross-resistance to Two Leading Drugs by
726 Distinct Mechanisms. *PLoS Negl Trop Dis* 10:e0005171.
- 727 47. Andersen JP, Vestergaard AL, Mikkelsen SA, Mogensen LS, Chalal M, Molday RS. 2016.
728 P4-ATPases as Phospholipid Flippases-Structure, Function, and Enigmas. *Front Physiol*
729 7:275.
- 730 48. Jeacock L, Baker N, Wiedemar N, Maser P, Horn D. 2017. Aquaglyceroporin-null
731 trypanosomes display glycerol transport defects and respiratory-inhibitor sensitivity. *PLoS*
732 *Pathog* 13:e1006307.
- 733 49. Uzcategui NL, Figarella K, Bassarak B, Meza NW, Mukhopadhyay R, Ramirez JL,
734 Duszenko M. 2013. *Trypanosoma brucei* aquaglyceroporins facilitate the uptake of arsenite
735 and antimonite in a pH dependent way. *Cell Physiol Biochem* 32:880-8.
- 736 50. Bassarak B, Uzcategui NL, Schonfeld C, Duszenko M. 2011. Functional characterization of
737 three aquaglyceroporins from *Trypanosoma brucei* in osmoregulation and glycerol
738 transport. *Cell Physiol Biochem* 27:411-20.
- 739 51. Jhingran A, Chawla B, Saxena S, Barrett MP, Madhubala R. 2009. Paromomycin: uptake
740 and resistance in *Leishmania donovani*. *Mol Biochem Parasitol* 164:111-7.

- 741 52. Shalev M, Kondo J, Kopelyanskiy D, Jaffe CL, Adir N, Baasov T. 2013. Identification of the
742 molecular attributes required for aminoglycoside activity against *Leishmania*. *Proc Natl*
743 *Acad Sci U S A* 110:13333-8.
- 744 53. Engstler M, Pfohl T, Herminghaus S, Boshart M, Wiegertjes G, Heddergott N, Overath P.
745 2007. Hydrodynamic flow-mediated protein sorting on the cell surface of trypanosomes.
746 *Cell* 131:505-15.
- 747 54. Alsford S, Field MC, Horn D. 2013. Receptor-mediated endocytosis for drug delivery in
748 African trypanosomes: fulfilling Paul Ehrlich's vision of chemotherapy. *Trends Parasitol*
749 29:207-12.
- 750 55. Sundar S, Sinha PK, Rai M, Verma DK, Nawin K, Alam S, Chakravarty J, Vaillant M, Verma
751 N, Pandey K, Kumari P, Lal CS, Arora R, Sharma B, Ellis S, Strub-Wourgaft N,
752 Balasegaram M, Oliario P, Das P, Modabber F. 2011. Comparison of short-course
753 multidrug treatment with standard therapy for visceral leishmaniasis in India: an open-label,
754 non-inferiority, randomised controlled trial. *Lancet* 377:477-86.
- 755 56. Musa A, Khalil E, Hailu A, Olobo J, Balasegaram M, Omollo R, Edwards T, Rashid J, Mbui
756 J, Musa B, Abuzaid AA, Ahmed O, Fadlalla A, El-Hassan A, Mueller M, Mucee G, Njoroje
757 S, Manduku V, Mutuma G, Apadet L, Lodenyo H, Mutea D, Kirigi G, Yifru S, Mengistu G,
758 Hurissa Z, Hailu W, Weldegebreal T, Tafes H, Mekonnen Y, Makonnen E, Ndegwa S,
759 Sagaki P, Kimutai R, Kesusu J, Owiti R, Ellis S, Wasunna M. 2012. Sodium stibogluconate
760 (SSG) & paromomycin combination compared to SSG for visceral leishmaniasis in East
761 Africa: a randomised controlled trial. *PLoS Negl Trop Dis* 6:e1674.
- 762 57. Venkatesh D, Boehm C, Barlow LD, Nankissoor NN, O'Reilly A, Kelly S, Dacks JB, Field
763 MC. 2017. Evolution of the endomembrane systems of trypanosomatids - conservation and
764 specialisation. *J Cell Sci* 130:1421-1434.
- 765 58. Diro E, Blesson S, Edwards T, Ritmeijer K, Fikre H, Admassu H, Kibret A, Ellis SJ,
766 Bardonneau C, Zijlstra EE, Soipei P, Mutinda B, Omollo R, Kimutai R, Omwalo G,
767 Wasunna M, Tadesse F, Alves F, Strub-Wourgaft N, Hailu A, Alexander N, Alvar J. 2019. A
768 randomized trial of AmBisome monotherapy and AmBisome and miltefosine combination to
769 treat visceral leishmaniasis in HIV co-infected patients in Ethiopia. *PLoS Negl Trop Dis*
770 13:e0006988.
- 771 59. Goyal V, Mahajan R, Pandey K, Singh SN, Singh RS, Strub-Wourgaft N, Alves F, Rabi Das
772 VN, Topno RK, Sharma B, Balasegaram M, Bern C, Hightower A, Rijal S, Ellis S, Sunyoto
773 T, Burza S, Lima N, Das P, Alvar J. 2018. Field safety and effectiveness of new visceral
774 leishmaniasis treatment regimens within public health facilities in Bihar, India. *PLoS Negl*
775 *Trop Dis* 12:e0006830.
- 776 60. Moreira RA, Mendanha SA, Fernandes KS, Matos GG, Alonso L, Dorta ML, Alonso A.
777 2014. Miltefosine increases lipid and protein dynamics in *Leishmania amazonensis*
778 membranes at concentrations similar to those needed for cytotoxicity activity. *Antimicrob*
779 *Agents Chemother* 58:3021-8.
- 780 61. Currier RB, Cooper A, Burrell-Saward H, MacLeod A, Alsford S. 2018. Decoding the
781 network of *Trypanosoma brucei* proteins that determines sensitivity to apolipoprotein-L1.
782 *PLoS Pathog* 14:e1006855.
- 783 62. Thomson R, Finkelstein A. 2015. Human trypanolytic factor APOL1 forms pH-gated cation-
784 selective channels in planar lipid bilayers: relevance to trypanosome lysis. *Proc Natl Acad*
785 *Sci U S A* 112:2894-9.
- 786 63. Vanwalleghem G, Fontaine F, Lecordier L, Tebabi P, Klewe K, Nolan DP, Yamaro-Botte
787 Y, Botte C, Kremer A, Burkard GS, Rassow J, Roditi I, Perez-Morga D, Pays E. 2015.
788 Coupling of lysosomal and mitochondrial membrane permeabilization in trypanolysis by
789 APOL1. *Nat Commun* 6:8078.
- 790 64. Shaw CD, Lonchamp J, Downing T, Imamura H, Freeman TM, Cotton JA, Sanders M,
791 Blackburn G, Dujardin JC, Rijal S, Khanal B, Illingworth CJ, Coombs GH, Carter KC. 2016.
792 In vitro selection of miltefosine resistance in promastigotes of *Leishmania donovani* from
793 Nepal: genomic and metabolomic characterization. *Mol Microbiol* 99:1134-48.
- 794 65. Coelho AC, Boisvert S, Mukherjee A, Leprohon P, Corbeil J, Ouellette M. 2012. Multiple
795 mutations in heterogeneous miltefosine-resistant *Leishmania major* population as
796 determined by whole genome sequencing. *PLoS Negl Trop Dis* 6:e1512.

- 797 66. Dean S, Sunter JD, Wheeler RJ. 2017. TrypTag.org: A Trypanosome Genome-wide Protein
798 Localisation Resource. *Trends Parasitol* 33:80-82.
- 799 67. Gray KC, Palacios DS, Dailey I, Endo MM, Uno BE, Wilcock BC, Burke MD. 2012.
800 Amphotericin primarily kills yeast by simply binding ergosterol. *Proc Natl Acad Sci U S A*
801 109:2234-9.
- 802 68. Belenky P, Camacho D, Collins JJ. 2013. Fungicidal drugs induce a common oxidative-
803 damage cellular death pathway. *Cell Rep* 3:350-8.
- 804 69. Purkait B, Kumar A, Nandi N, Sardar AH, Das S, Kumar S, Pandey K, Ravidas V, Kumar M,
805 De T, Singh D, Das P. 2012. Mechanism of amphotericin B resistance in clinical isolates of
806 *Leishmania donovani*. *Antimicrob Agents Chemother* 56:1031-41.
- 807 70. Pountain AW, Weidt SK, Regnault C, Bates PA, Donachie AM, Dickens NJ, Barrett MP.
808 2019. Genomic instability at the locus of sterol C24-methyltransferase promotes
809 amphotericin B resistance in *Leishmania* parasites. *PLoS Negl Trop Dis* 13:e0007052.
- 810 71. Alsford S, Kawahara T, Glover L, Horn D. 2005. Tagging a *T. brucei* RNA locus improves
811 stable transfection efficiency and circumvents inducible expression position effects. *Mol*
812 *Biochem Parasitol* 144:142-8.
- 813 72. Schumann Burkard G, Jutzi P, Roditi I. 2011. Genome-wide RNAi screens in bloodstream
814 form trypanosomes identify drug transporters. *Mol Biochem Parasitol* 175:91-4.
- 815 73. Alsford S, Horn D. 2008. Single-locus targeting constructs for reliable regulated RNAi and
816 transgene expression in *Trypanosoma brucei*. *Mol Biochem Parasitol* 161:76-9.
- 817 74. Raz B, Iten M, Grether-Buhler Y, Kaminsky R, Brun R. 1997. The Alamar Blue assay to
818 determine drug sensitivity of African trypanosomes (*T. b. rhodesiense* and *T. b. gambiense*)
819 in vitro. *Acta Trop* 68:139-47.
- 820 75. Langmead B, Trapnell C, Pop M, Salzberg SL. 2009. Ultrafast and memory-efficient
821 alignment of short DNA sequences to the human genome. *Genome Biol* 10:R25.
- 822 76. Li H, Handsaker B, Wysoker A, Fennell T, Ruan J, Homer N, Marth G, Abecasis G, Durbin
823 R, Genome Project Data Processing S. 2009. The Sequence Alignment/Map format and
824 SAMtools. *Bioinformatics* 25:2078-9.
- 825 77. Rutherford K, Parkhill J, Crook J, Horsnell T, Rice P, Rajandream MA, Barrell B. 2000.
826 Artemis: sequence visualization and annotation. *Bioinformatics* 16:944-5.
- 827 78. Huson DH, Scornavacca C. 2012. Dendroscope 3: an interactive tool for rooted
828 phylogenetic trees and networks. *Syst Biol* 61:1061-7.
- 829 79. Tsirigos KD, Peters C, Shu N, Kall L, Elofsson A. 2015. The TOPCONS web server for
830 consensus prediction of membrane protein topology and signal peptides. *Nucleic Acids Res*
831 43:W401-7.
- 832 80. Redmond S, Vadivelu J, Field MC. 2003. RNAit: an automated web-based tool for the
833 selection of RNAi targets in *Trypanosoma brucei*. *Mol Biochem Parasitol* 128:115-8.
- 834 81. Alsford S, Currier RB, Guerra-Assuncao JA, Clark TG, Horn D. 2014. Cathepsin-L can
835 resist lysis by human serum in *Trypanosoma brucei brucei*. *PLoS Pathog* 10:e1004130.

836

837

838 **Figure legends**

839

840 **Figure 1**

841 **Anti-leishmanial drug selection of a genome-scale *T. brucei* RNAi library. A)**

842 Representative EC₅₀ charts showing the susceptibility of *T. brucei* to the anti-leishmanial
843 drugs. Individual EC₅₀ assays were carried out in quadruplicate; error bars represent
844 standard deviation. Insets: structures of the anti-leishmanial drugs

845 (www.Chemspider.com). B) Schematic showing bloodstream-form *T. brucei* RNAi library
846 selection and RNAi fragment identification by RIT-seq. C) Growth during anti-leishmanial
847 drug selection of the BSF *T. brucei* RNAi library; selection was initiated in 1.5X EC₅₀,
848 except for miltefosine (1.0X EC₅₀), and adjusted as indicated (black arrows); induction in 1
849 µg.ml⁻¹ tetracycline was maintained throughout. Genomic DNA prepared at the indicated
850 times (red arrows). Insets: RNAi library-specific PCR.

851

852 **Figure 2**

853 **Genome-scale maps showing hits in each screen.** Illumina sequencing of the amplified
854 RNAi target fragments identifies *T. brucei* orthologues of known *Leishmania* drug
855 transporters and novel putative drug efficacy determinants. RNAi fragments amplified from
856 each selective screen were mapped against the TREU927 *T. brucei* reference genome.

857 Red bars correspond to *T. brucei* orthologues of known *Leishmania* drug transporters:
858 *AQP2-3*, aquaglyceroporin-2-3 locus, Tb927.10.14160-70; *MT*, miltefosine transporter
859 orthologue, Tb927.11.3350. The y-axes are truncated to 10⁴ reads/kilobase/transcript.

860 SSG, sodium stibogluconate; Pmm, paromomycin; Milt, miltefosine; AmB, amphotericin-B.

861

862 **Figure 3**

863 **TbAQP3, a *T. brucei* orthologue of *Leishmania* AQP1, is selective for sodium**
864 **stibogluconate.** A) Total (red) and RNAi construct-specific 14mer-containing (blue) reads
865 mapping to the *TbAQP2-3* locus, Tb927.10.14160-70. Targeted open reading frames
866 highlighted in green; flanking open reading frames coloured grey. B) Sodium
867 stibogluconate EC₅₀ assay following deletion of the *T. brucei* AQP2-3 locus (*aqp2-3*). C)
868 Sodium stibogluconate and D) pentamidine EC₅₀ assays following expression of ^{GFP}AQP2
869 (left panels) and ^{GFP}AQP3 (right panels) in *aqp2-3* null *T. brucei*. Individual EC₅₀ assays
870 were carried out in quadruplicate. Error bars represent standard deviation. WT, *T. brucei*
871 wild type for the AQP2-3 locus.

872

873 **Figure 4**

874 **The *T. brucei* lysosomal major facilitator superfamily protein influences the efficacy**
875 **of aminoglycoside drugs.** A) Total (red) and RNAi construct-specific 14mer-containing
876 (blue) reads mapping to the *MFST* locus, Tb927.9.6360-80. Targeted open reading frames
877 highlighted in green; flanking open reading frames coloured grey. B) Unrooted neighbour
878 joining tree comparing representative *Leishmania* MFST proteins with Tb927.9.6360-80
879 (highlighted in green; see Fig. S3 for extended tree). C) Predicted *trans*-membrane
880 organisation of the Tb927.9.6360-80 proteins and the selected *Leishmania* proteins (TM
881 domains, vertical bars). D) *MFST* locus deletion strategy and Southern hybridisation
882 confirming generation of heterozygous (-/+) and homozygous (-/-) *MFST* locus null *T.*
883 *brucei*. X, *Xho*I; D, deletion probe; F, flanking probe; *PAC*, puromycin acetyltransferase;
884 *BSD*, blasticidin S-deaminase; WT, wild type. E) Growth of WT and *MFST* locus null (*mfst*)
885 *T. brucei* in culture. F-H) Representative EC₅₀ assays comparing the sensitivity of WT and
886 *mfst T. brucei* to F) suramin, G) paromomycin and H) neomycin. Inset charts summarise
887 EC₅₀ data from three independent biological replicates. Individual growth (E) and EC₅₀ (F-

888 H) assays were carried out in triplicate and quadruplicate, respectively. Error bars
889 represent standard deviation. *P*-values derived from Student's *t*-test (** *P*<0.01).

890

891 **Figure 5**

892 **Pairwise comparisons identify putative amphotericin-B/miltefosine cross-efficacy**

893 **loci.** Pairwise comparisons of the sequenced outputs from the four selective screens. Data
894 converted to reads per kilobase per million mapped reads (RPKM) to control for minor
895 inter-library variations in read depth. Dashed lines represent stringent 100-read cut offs for
896 each selected RNAi library converted to RPKM. High confidence cross-efficacy
897 determinants highlighted in red in the top right quadrant following comparison of the
898 miltefosine and amphotericin-B selected RNAi libraries.

899

900 **Figure 6**

901 ***T. brucei* VAMP7B, Tb927.5.3560, and the action of amphotericin-B and miltefosine.**

902 A) Total (red) and RNAi construct-specific 14mer-containing (blue) reads mapping to
903 *Tb927.5.3550-70* following amphotericin-B and miltefosine selection. Targeted open
904 reading frames highlighted in green; flanking open reading frames coloured grey. B) *T.*
905 *brucei* population growth following TbVAMP7B (Tb927.5.3560) RNAi knockdown. Inset:
906 confirmation of RNAi knockdown by northern blot following 24-hour induction in 1 $\mu\text{g.ml}^{-1}$
907 tetracycline; ethidium bromide stained gel shown as a loading control. C) Representative
908 30-hour amphotericin-B EC_{50} assay following TbVAMP7B RNAi knockdown induced in 2
909 ng.ml^{-1} tetracycline. Inset chart summarises Hill coefficient data for five biological
910 replicates. D) The effect of TbVAMP7B RNAi knockdown on EC_x for five biological
911 replicates; data derived for each replicate from EC_{50} values and Hill coefficients presented
912 in (C). E) Representative 30-hour miltefosine EC_{50} assay following TbVAMP7B RNAi
913 knockdown induced in 2 ng.ml^{-1} tetracycline; data plotted to show population growth

914 relative to untreated *T. brucei* (uninduced or induced). Dashed ellipse highlights
915 miltefosine-mediated complementation of the Tb927.5.3560 RNAi growth defect. F) Chart
916 summarising *T. brucei* population growth in the presence or absence of TbVAMP7B RNAi
917 in a subset of miltefosine concentrations from five independent biological replicates.
918 Individual growth (B) and EC₅₀ (C, E) assays were carried out in triplicate and
919 quadruplicate, respectively. Error bars represent standard deviation. *P*-values derived from
920 paired Student's *t*-test (** <0.01; *** <0.001).

921

922 **Figure 7**

923 **The *T. brucei* miltefosine transporter orthologue, Tb927.11.3350, influences**
924 **miltefosine and amphotericin-B efficacy against *T. brucei*.** A) Total (red) and RNAi
925 construct-specific 14mer-containing (blue) reads mapping to *Tb927.11.3350* following
926 amphotericin-B (AmB) or miltefosine selection. Targeted open reading frames highlighted
927 in green; flanking open reading frames coloured grey. B) *T. brucei* population growth
928 following RNAi knockdown of Tb927.11.3350. Inset: confirmation of RNAi knockdown by
929 northern blot; ethidium bromide stained gel shown as a loading control. C, D)
930 Representative amphotericin-B and miltefosine EC₅₀ assays following RNAi knockdown of
931 Tb927.11.3350. Inset charts summarise data from three independent biological replicates.
932 Individual growth (B) and EC₅₀ (C, D) assays were carried out in triplicate and
933 quadruplicate, respectively. Error bars represent standard deviation. *P*-values derived from
934 Student's *t*-test (* <0.05; ** <0.01). RNAi inductions were carried out in 1 µg.ml⁻¹
935 tetracycline.

936

937 **Figure 8**

938 **Flippases influence the action of amphotericin-B.** A) Neighbour joining phylogenetic
939 tree showing the *T. brucei* and *L. major* flippases versus the *S. cerevisiae* flippases

940 (Neo1p, Drs2p and DNF1-3) and a representative cation-transporting P-type ATPase
941 (Pay2). Schematics of predicted *T. brucei* and *L. major* flippases and representative *S.*
942 *cerevisiae* flippases (Neo1p and DNF3) and P-type ATPase (Pay2), highlighting key
943 conserved residues (actuator domain: TGES [green triangle], DEGT [pink triangle]; and,
944 phosphorylation domain, DKTGT [yellow triangle]); predicted signal peptide, vertical red
945 bar; and, predicted *trans*-membrane domain organisation, vertical black bars. B) Total
946 (red) and RNAi construct-specific 14mer-containing (blue) reads mapping to
947 *Tb927.11.13000* and *Tb927.6.3550* following amphotericin-B selection. Targeted open
948 reading frames highlighted in green; flanking open reading frames coloured grey. C) *T.*
949 *brucei* population growth following RNAi knockdown of *Tb927.11.13000*. Inset:
950 confirmation of RNAi knockdown by northern blot; ethidium bromide stained gel shown as
951 a loading control. D, E) Representative amphotericin-B and miltefosine EC₅₀ assays
952 following RNAi knockdown of *Tb927.11.13000*. Inset charts summarise data from three
953 independent biological replicates. Individual growth (C) and EC₅₀ (D, E) assays were
954 carried out in triplicate and quadruplicate, respectively. Error bars represent standard
955 deviation. *P*-values derived from Student's *t*-test (* <0.05; ** <0.01). RNAi inductions were
956 carried out in 1 µg.ml⁻¹ tetracycline, unless otherwise stated.

957

958 **Figure 9**

959 **Known and candidate drivers of anti-leishmanial drug efficacy in *Leishmania*.** The
960 key *T. brucei* proteins identified in our anti-leishmanial loss-of-function screen (left hand
961 panel) and their *Leishmania* orthologues (right hand panel) represent candidate anti-
962 leishmanial drug efficacy determinants. Red denotes known *Leishmania* drivers of anti-
963 leishmanial efficacy whose loss-of-function reduces drug efficacy (see text for details). The
964 strain prefix for the truncated gene IDs is at the top of each panel, with the exception of the
965 sterol biosynthetic enzymes recently shown to contribute to amphotericin-B efficacy

966 against *L. mexicana* (70). Grey-filled circles (endosomes) and ellipses (lysosome)
967 represent the endocytic system. The purple block represents membrane modified by
968 changes in sterol biosynthesis and the putative action of the flippases and their β -subunit;
969 changes in membrane composition anywhere in the endocytic system may influence the
970 intracellular transit of amphotericin-B or its ability to form ion permeable channels.

971

972 **Figure S1**

973 **Candidate anti-leishmanial drug efficacy determinants identified by *T. brucei* RNAi**
974 **library selection.** Total (red) and RNAi construct-specific 14mer-containing (blue) reads
975 mapping to individual loci following BSF *T. brucei* RNA library selection in paromomycin
976 (A), amphotericin-B (B) and miltefosine (C). Targeted open reading frames highlighted in
977 green; flanking open reading frames coloured grey. Where a substantial number of reads
978 target regions outside the open reading frame, the predicted untranslated region is
979 highlighted by a narrow green bar. See Table S1 for further details.

980

981 **Figure S2**

982 **Neither AAT15 (Tb927.11.6680) depletion nor Tudor Staphylococcal nuclease**
983 **(Tb927.11.14190) deletion affects aminoglycoside efficacy against BSF *T. brucei***
984 **over 72 hours.** A, B) Total (red) and RNAi construct-specific 14mer-containing (blue)
985 reads mapping to *Tb927.11.6680* (A) and *Tb927.11.14190* (B) following paromomycin
986 selection. Targeted open reading frames highlighted in green; flanking open reading
987 frames coloured grey. C) *T. brucei* population growth following AAT15 RNAi knockdown.
988 Inset: RNA depletion was confirmed by RT-qPCR following 24-hour induction in $1 \mu\text{g.ml}^{-1}$
989 tetracycline. D, E) Representative paromomycin and neomycin EC_{50} assays following
990 AAT15 RNAi knockdown induced in $1 \mu\text{g.ml}^{-1}$ tetracycline. F, G) Representative
991 paromomycin (D) and neomycin (E) EC_{50} assays comparing wild type and

992 *Tb927.11.14190* null (*tsn*) BSF *T. brucei*. Inset charts summarise data from three
993 independent biological replicates. Individual growth (C) and EC₅₀ (D-G) assays were
994 carried out in triplicate and quadruplicate, respectively. Error bars represent standard
995 deviation.

996

997 **Figure S3**

998 ***Tb927.9.6360-80* clusters with the syntenic *LmjF.15.0870*.** Twenty nine open reading
999 frames annotated 'major facilitator' or 'MFS' in the *L. major* Friedlin reference genome
1000 were aligned with the *Tb927.9.6360-80* open reading frames using Clustal Omega
1001 (<https://www.ebi.ac.uk/Tools/msa/clustalo/>). The unrooted neighbour joining phylogenetic
1002 tree was formatted in Dendroscope 3 (<http://dendroscope.org/>).

1003

1004 **Figure S4**

1005 ***MFST* locus null *T. brucei* exhibit enhanced tolerance to high concentration**
1006 **aminoglycosides.** Relative population growth of wild type (WT) and *MFST* locus null
1007 (*mfst*) *T. brucei* in A) paromomycin and B) neomycin at >EC₉₉. Assays were carried out in
1008 triplicate. Error bars represent standard deviation.

1009

1010 **Figure S5**

1011 ***Tb927.5.3570* does not contribute to the efficacy of amphotericin-B or miltefosine**
1012 **against *T. brucei*.** A) *T. brucei* population growth following *Tb927.5.3570* RNAi
1013 knockdown. Inset: confirmation of RNAi knockdown by northern blot; ethidium bromide
1014 stained gel shown as a loading control. B, C) Representative amphotericin-B and
1015 miltefosine EC₅₀ assays following *Tb927.5.3570* RNAi knockdown. RNAi inductions were
1016 carried out in 1 µg.ml⁻¹ tetracycline. Individual growth (A) and EC₅₀ (B, C) assays were

1017 carried out in triplicate and quadruplicate, respectively. Error bars represent standard
1018 deviation.

1019

1020 **Figure S6**

1021 **Gene Ontology analysis of the high confidence hits identified following**
1022 **amphotericin-B RNAi library selection.** Plot generated using the GO analysis tool at
1023 TritypDB.org. Point diameter corresponds to relative number of proteins in each category.
1024 See Table S2 for further details.

1025

1026 **Figure S7**

1027 ***T. brucei* exhibit enhanced tolerance to high concentration amphotericin-B following**
1028 **flippase depletion.** A, C) Representative assays showing relative population growth in
1029 $>EC_{99}$ amphotericin-B following (A) Tb927.11.3350 and (C) Tb927.11.13000 RNAi
1030 knockdown. B, D) Relative population growth in $>EC_{99}$ amphotericin-B following (B)
1031 Tb927.11.3350 and (D) Tb927.11.13000 RNAi knockdown; data derived from three
1032 independent biological replicates. Individual growth assays were carried out in triplicate.
1033 Error bars represent standard deviation. *P*-values derived from Student's *t*-test (* <0.05 ;
1034 *** <0.001). RNAi inductions were carried out in $1 \mu\text{g.ml}^{-1}$ tetracycline.

1035

1036 **Table S1**

1037 Transcripts represented by >99 RNAi construct-specific barcode-containing reads per
1038 kilobase per transcript following BSF *T. brucei* RNAi library selection in the anti-leishmanial
1039 drugs.

1040

1041 **Table S2**

1042 Gene Ontology analysis of the high confidence hits identified by amphotericin-B RNAi
1043 library selection.

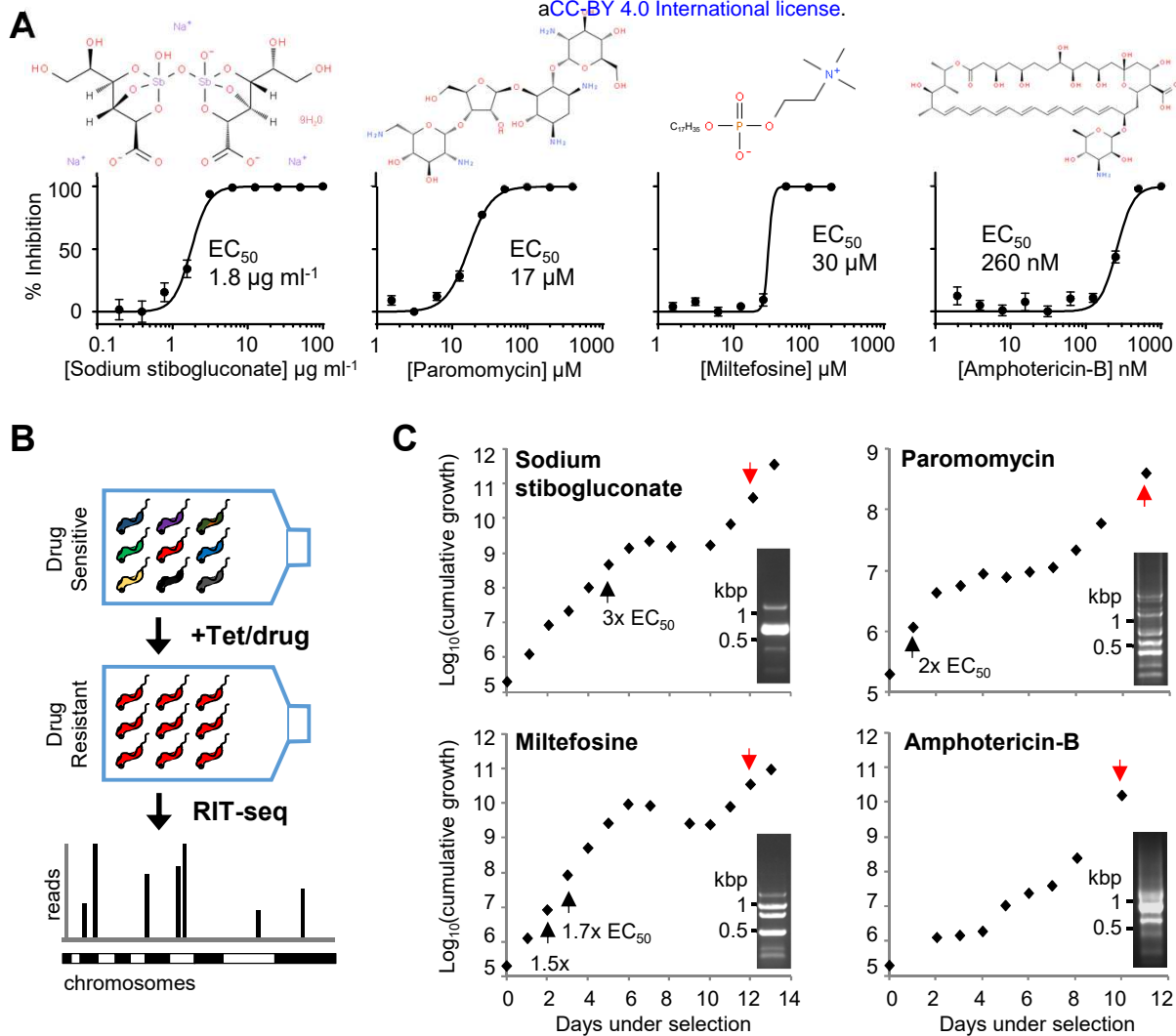
1044

1045 **Acknowledgements**

1046 This work was funded by a Wellcome Trust Institutional Strategic Support Fund (LSHTM)
1047 fellowship (www.wellcome.ac.uk/) awarded to SA. DH is a Wellcome Trust Investigator
1048 award recipient (100320/Z/12/Z). HBSS was supported by the Biotechnology and
1049 Biological Sciences Research Council (BB/J014567/1). MVS was supported by the
1050 Leonardo da Vinci internship programme. The funders had no role in study design, data
1051 collection and interpretation, or the decision to submit the work for publication. Thanks to
1052 Dr Vanessa Yardley, LSHTM, for sharing her stocks of the anti-leishmanial drugs, sodium
1053 stibogluconate, miltefosine and amphotericin-B. Thanks to the 'Advanced training in
1054 molecular biology' (LSHTM) class of 2017 for the *MFST* null Southern images.

Figure 1

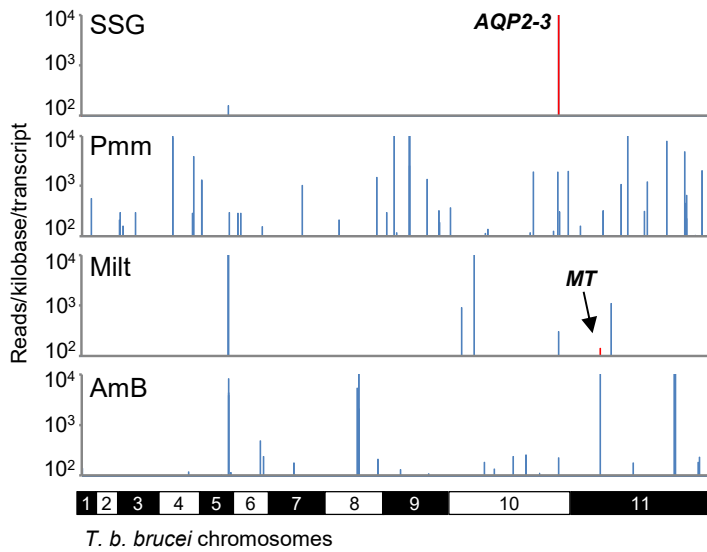
bioRxiv preprint doi: <https://doi.org/10.1101/605873>; this version posted April 13, 2019. The copyright holder for this preprint (which was not certified by peer review) is the author/funder, who has granted bioRxiv a license to display the preprint in perpetuity. It is made available under aCC-BY 4.0 International license.



Anti-leishmanial drug selection of a genome-scale *T. brucei* RNAi library. A) Representative EC₅₀ charts showing the susceptibility of *T. brucei* to the anti-leishmanial drugs. Individual EC₅₀ assays were carried out in quadruplicate; error bars represent standard deviation. Insets: structures of the anti-leishmanial drugs (www.ChempSpider.com). B) Schematic showing bloodstream-form *T. brucei* RNAi library selection and RNAi fragment identification by RIT-seq. C) Growth during anti-leishmanial drug selection of the BSF *T. brucei* RNAi library; selection was initiated in 1.5X EC₅₀, except for miltefosine (1.0X EC₅₀), and adjusted as indicated (black arrows); induction in 1 μg.ml⁻¹ tetracycline was maintained throughout. Genomic DNA prepared at the indicated times (red arrows). Insets: RNAi library-specific PCR.

Figure 2

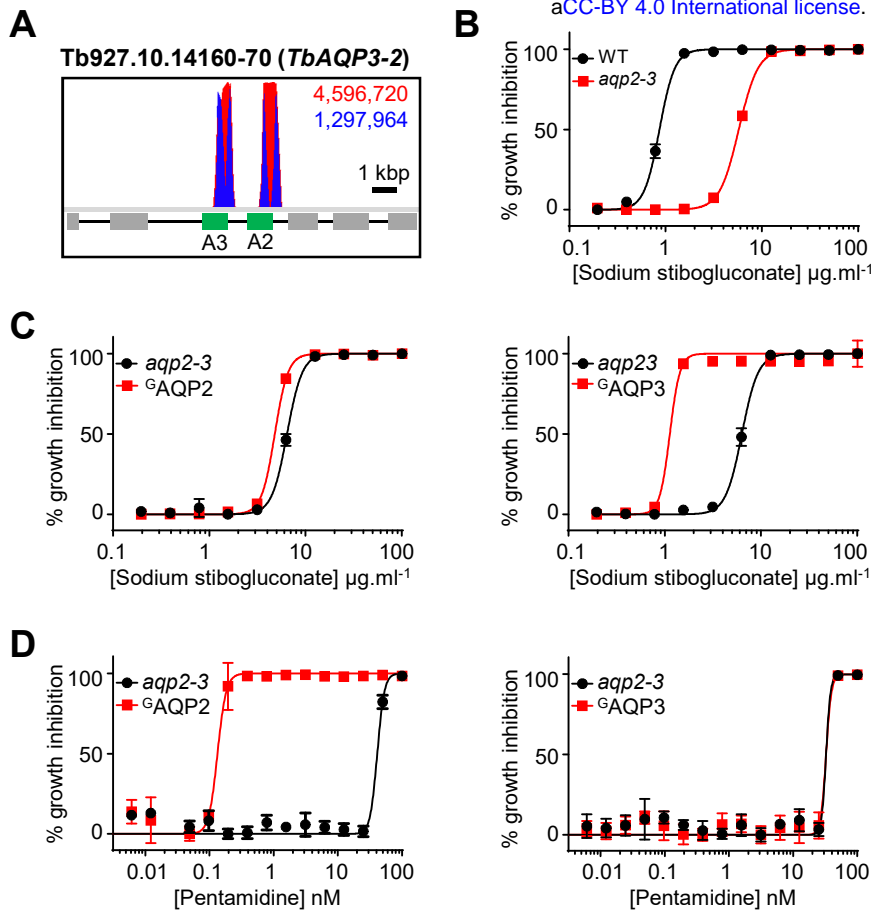
bioRxiv preprint doi: <https://doi.org/10.1101/605873>; this version posted April 13, 2019. The copyright holder for this preprint (which was not certified by peer review) is the author/funder, who has granted bioRxiv a license to display the preprint in perpetuity. It is made available under aCC-BY 4.0 International license.



Genome-scale maps showing hits in each screen. Illumina sequencing of the amplified RNAi target fragments identifies *T. brucei* orthologues of known *Leishmania* drug transporters and novel putative drug efficacy determinants. RNAi fragments amplified from each selective screen were mapped against the TREU927 *T. brucei* reference genome. Red bars correspond to *T. brucei* orthologues of known *Leishmania* drug transporters: *AQP2-3*, aquaglyceroporin-2-3 locus, Tb927.10.14160-70; *MT*, miltefosine transporter orthologue, Tb927.11.3350. The y-axes are truncated to 10^4 reads/kilobase/transcript. SSG, sodium stibogluconate; Pmm, paromomycin; Milt, miltefosine; AmB, amphotericin-B.

Figure 3

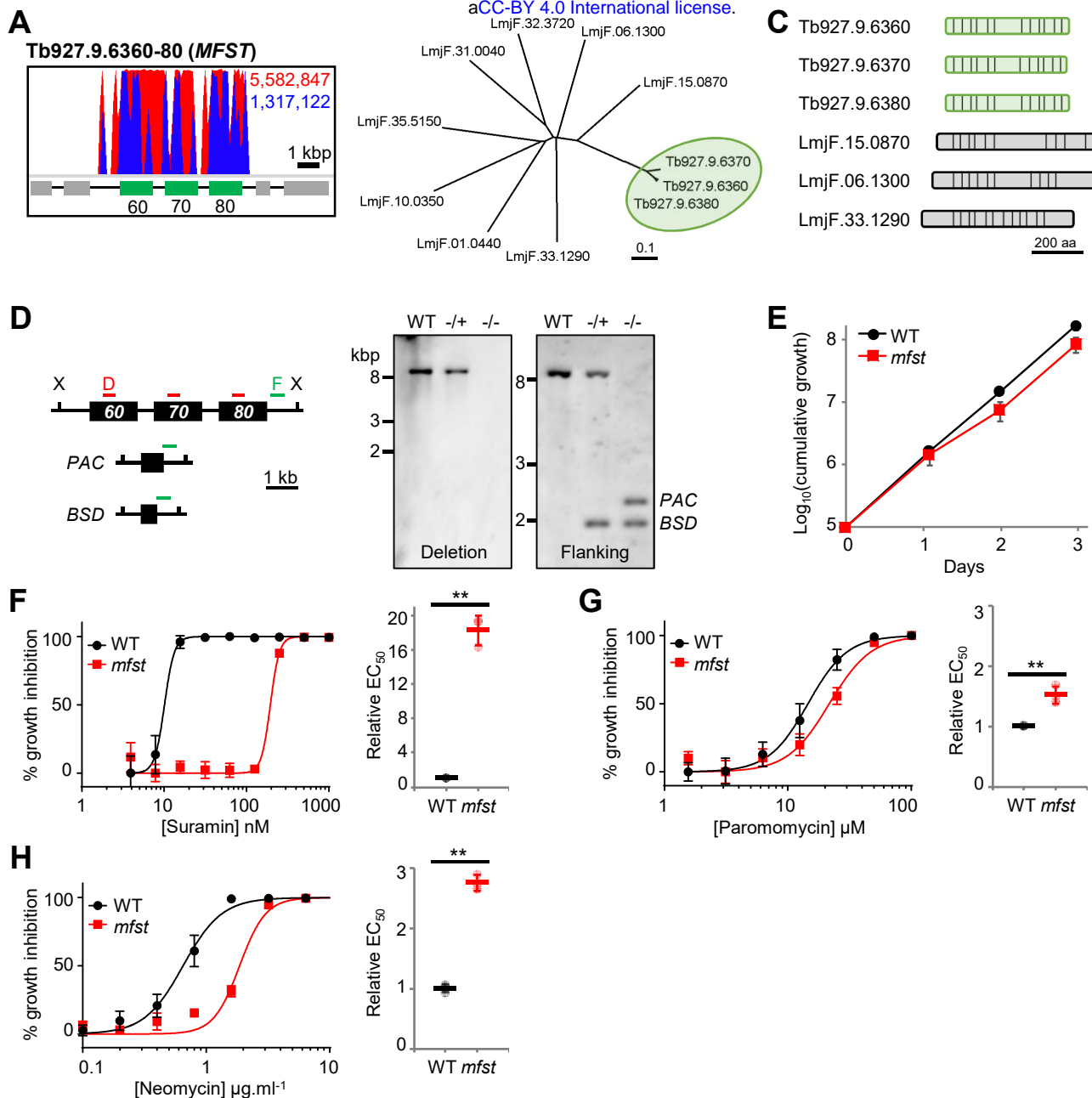
bioRxiv preprint doi: <https://doi.org/10.1101/605873>; this version posted April 13, 2019. The copyright holder for this preprint (which was not certified by peer review) is the author/funder, who has granted bioRxiv a license to display the preprint in perpetuity. It is made available under aCC-BY 4.0 International license.



TbAQP3, a *T. brucei* orthologue of *Leishmania* AQP1, is selective for sodium stibogluconate. A) Total (red) and RNAi construct-specific 14mer-containing (blue) reads mapping to the *TbAQP2-3* locus, Tb927.10.14160-70. Targeted open reading frames highlighted in green; flanking open reading frames coloured grey. B) Sodium stibogluconate EC₅₀ assay following deletion of the *T. brucei* AQP2-3 locus (*aqp2-3*). C) Sodium stibogluconate and D) pentamidine EC₅₀ assays following expression of ^{GFP}AQP2 (left panels) and ^{GFP}AQP3 (right panels) in *aqp2-3* null *T. brucei*. Individual EC₅₀ assays were carried out in quadruplicate. Error bars represent standard deviation. WT, *T. brucei* wild type for the AQP2-3 locus.

Figure 4

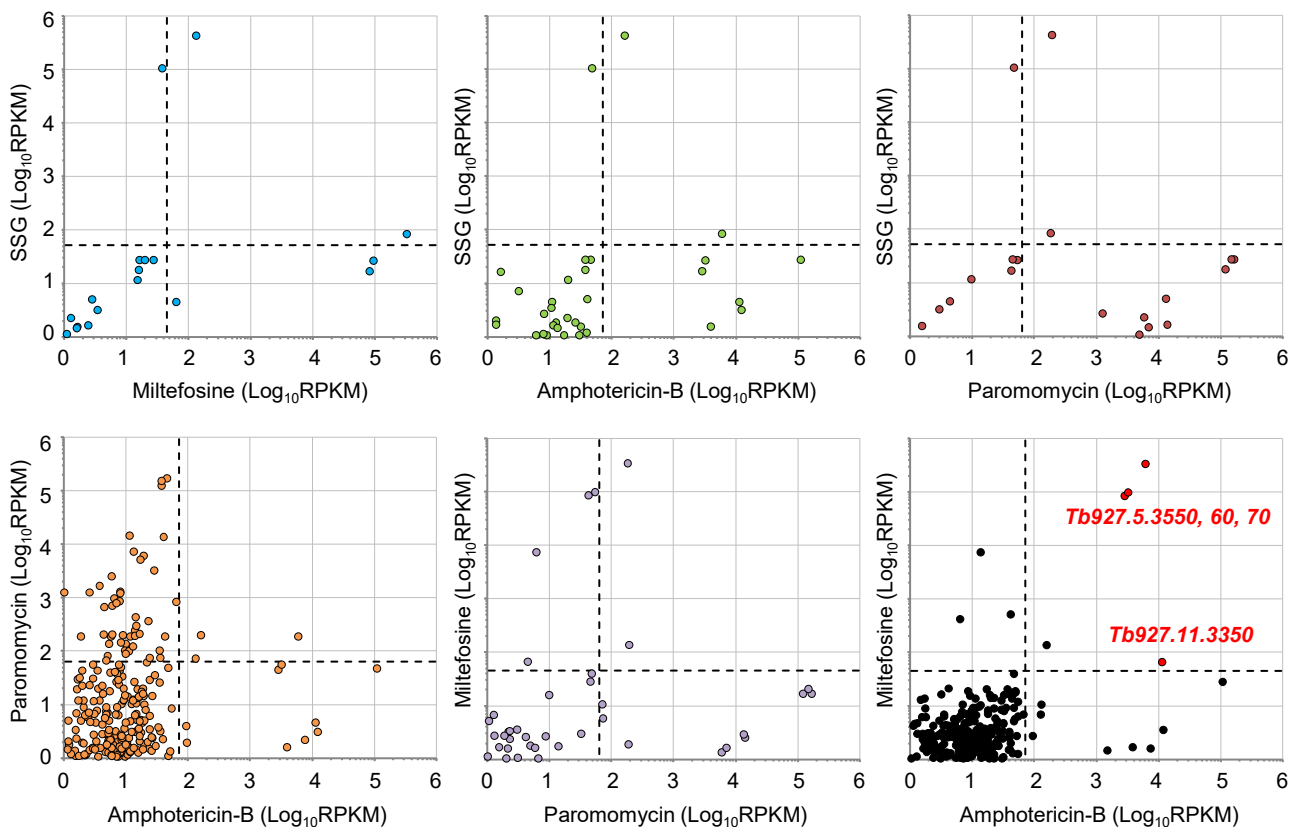
bioRxiv preprint doi: <https://doi.org/10.1101/605873>; this version posted April 13, 2019. The copyright holder for this preprint (which was not certified by peer review) is the author/funder, who has granted bioRxiv a license to display the preprint in perpetuity. It is made available under aCC-BY 4.0 International license.



The *T. brucei* lysosomal major facilitator superfamily protein influences the efficacy of aminoglycoside drugs. A) Total (red) and RNAi construct-specific 14mer-containing (blue) reads mapping to the *MFST* locus, *Tb927.9.6360-80*. Targeted open reading frames highlighted in green; flanking open reading frames coloured grey. B) Unrooted neighbour joining tree comparing representative *Leishmania* MFST proteins with *Tb927.9.6360-80* (highlighted in green; see Fig. S3 for extended tree). C) Predicted *trans*-membrane organisation of the *Tb927.9.6360-80* proteins and the selected *Leishmania* proteins (TM domains, vertical bars). D) *MFST* locus deletion strategy and Southern hybridisation confirming generation of heterozygous (-/+) and homozygous (-/-) *MFST* locus null *T. brucei*. X, *Xho*I; D, deletion probe; F, flanking probe; PAC, puromycin acetyltransferase; BSD, blasticidin S-deaminase; WT, wild type. E) Growth of WT and *MFST* locus null (*mfst*) *T. brucei* in culture. F-H) Representative EC₅₀ assays comparing the sensitivity of WT and *mfst* *T. brucei* to F) suramin, G) paromomycin and H) neomycin. Inset charts summarise EC₅₀ data from three independent biological replicates. Individual growth (E) and EC₅₀ (F-H) assays were carried out in triplicate and quadruplicate, respectively. Error bars represent standard deviation. *P*-values derived from Student's *t*-test (** *P*<0.01).

Figure 5

bioRxiv preprint doi: <https://doi.org/10.1101/605873>; this version posted April 13, 2019. The copyright holder for this preprint (which was not certified by peer review) is the author/funder, who has granted bioRxiv a license to display the preprint in perpetuity. It is made available under aCC-BY 4.0 International license.

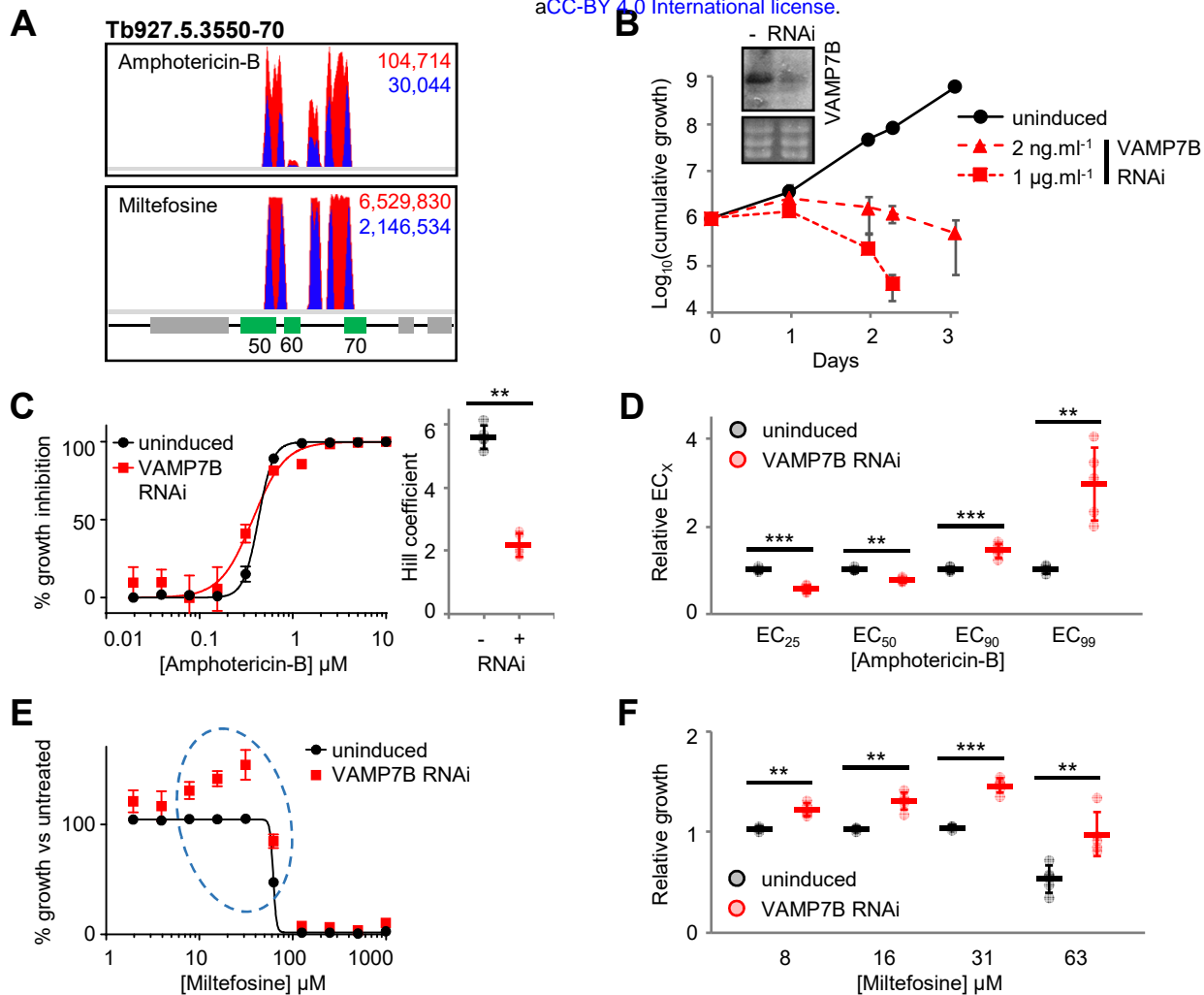


Pairwise comparisons identify putative amphotericin-B miltefosine cross-efficacy loci.

Pairwise comparisons of the sequenced outputs from the four selective screens. Data converted to reads per kilobase per million mapped reads (RPKM) to control for minor inter-library variations in read depth. Dashed lines represent stringent 100-read cut offs for each selected RNAi library converted to RPKM. High confidence cross-efficacy determinants highlighted in red in the top right quadrant following comparison of the miltefosine and amphotericin-B selected RNAi libraries.

Figure 6

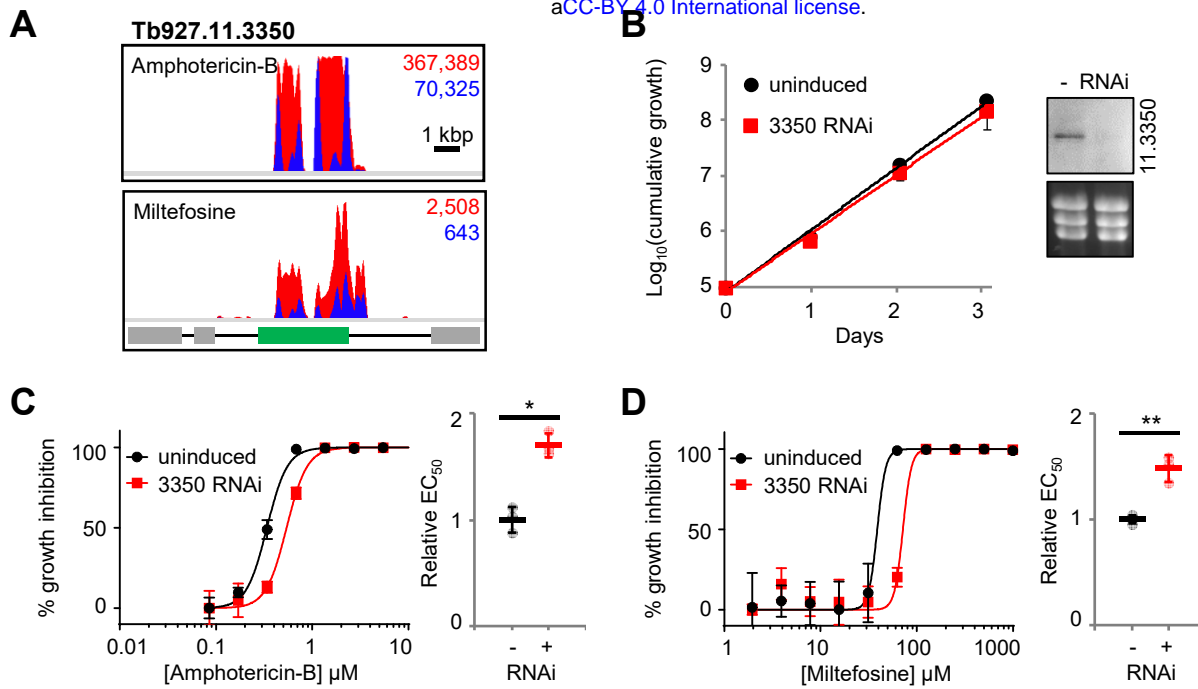
bioRxiv preprint doi: <https://doi.org/10.1101/605873>; this version posted April 13, 2019. The copyright holder for this preprint (which was not certified by peer review) is the author/funder, who has granted bioRxiv a license to display the preprint in perpetuity. It is made available under aCC-BY 4.0 International license.



T. brucei VAMP7B, Tb927.5.3560, and the action of amphotericin-B and miltefosine. A) Total (red) and RNAi construct-specific 14mer-containing (blue) reads mapping to *Tb927.5.3550-70* following amphotericin-B and miltefosine selection. Targeted open reading frames highlighted in green; flanking open reading frames coloured grey. B) *T. brucei* population growth following TbVAMP7B (Tb927.5.3560) RNAi knockdown. Inset: confirmation of RNAi knockdown by northern blot following 24-hour induction in 1 $\mu\text{g}.\text{ml}^{-1}$ tetracycline; ethidium bromide stained gel shown as a loading control. C) Representative 30-hour amphotericin-B EC_{50} assay following TbVAMP7B RNAi knockdown induced in 2 $\text{ng}.\text{ml}^{-1}$ tetracycline. Inset chart summarises Hill coefficient data for five biological replicates. D) The effect of TbVAMP7B RNAi knockdown on EC_x for five biological replicates; data derived for each replicate from EC_{50} values and Hill coefficients presented in (C). E) Representative 30-hour miltefosine EC_{50} assay following TbVAMP7B RNAi knockdown induced in 2 $\text{ng}.\text{ml}^{-1}$ tetracycline; data plotted to show population growth relative to untreated *T. brucei* (uninduced or induced). Dashed ellipse highlights miltefosine-mediated complementation of the Tb927.5.3560 RNAi growth defect. F) Chart summarising *T. brucei* population growth in the presence or absence of TbVAMP7B RNAi in a subset of miltefosine concentrations from five independent biological replicates. Individual growth (B) and EC_{50} (C, E) assays were carried out in triplicate and quadruplicate, respectively. Error bars represent standard deviation. *P*-values derived from paired Student's *t*-test (** < 0.01; *** < 0.001).

Figure 7

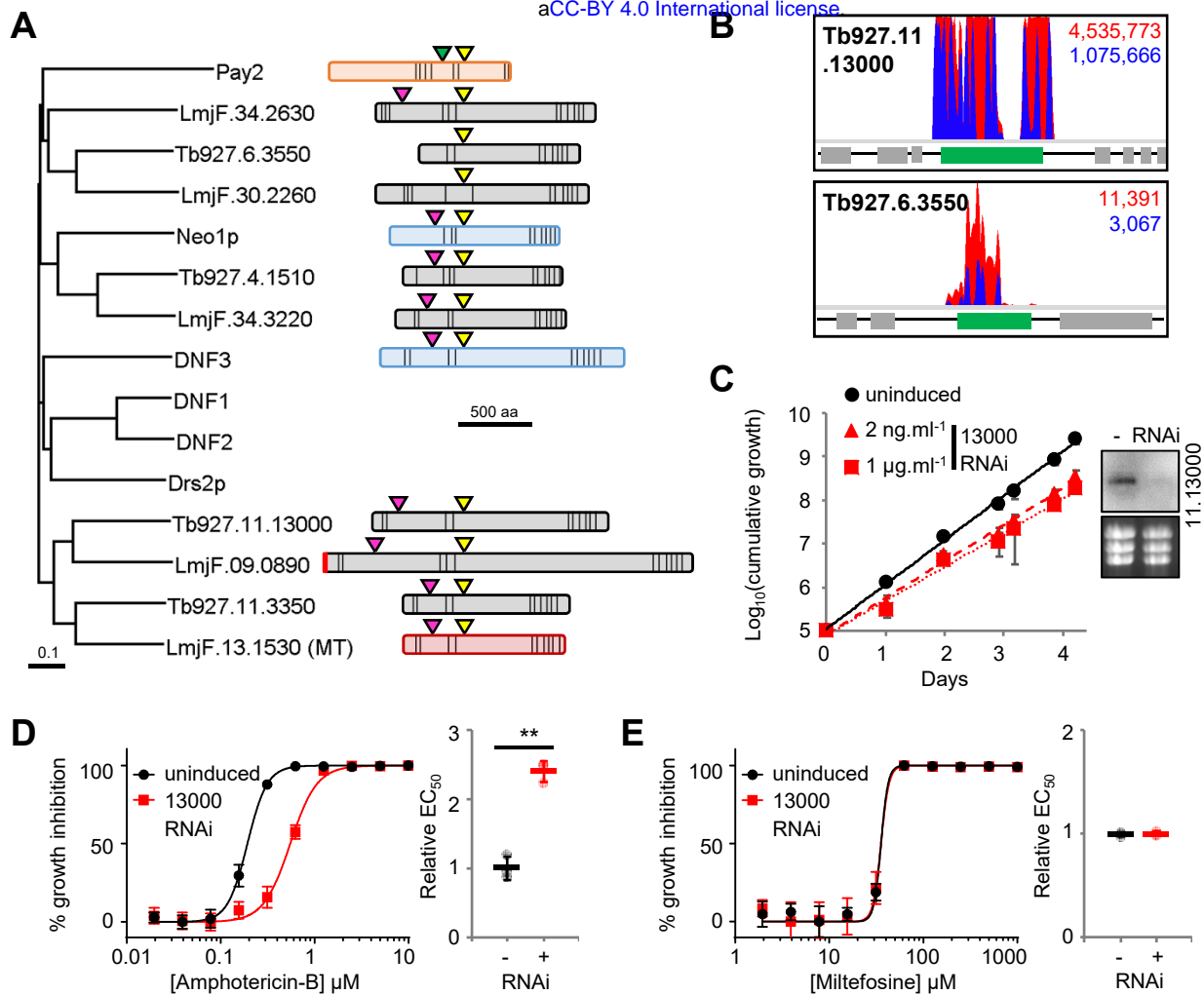
bioRxiv preprint doi: <https://doi.org/10.1101/605873>; this version posted April 13, 2019. The copyright holder for this preprint (which was not certified by peer review) is the author/funder, who has granted bioRxiv a license to display the preprint in perpetuity. It is made available under aCC-BY 4.0 International license.



The *T. brucei* miltefosine transporter orthologue, Tb927.11.3350, influences miltefosine and amphotericin-B efficacy against *T. brucei*. A) Total (red) and RNAi construct-specific 14mer-containing (blue) reads mapping to *Tb927.11.3350* following amphotericin-B (AmB) or miltefosine selection. Targeted open reading frames highlighted in green; flanking open reading frames coloured grey. B) *T. brucei* population growth following RNAi knockdown of *Tb927.11.3350*. Inset: confirmation of RNAi knockdown by northern blot; ethidium bromide stained gel shown as a loading control. C, D) Representative amphotericin-B and miltefosine EC₅₀ assays following RNAi knockdown of *Tb927.11.3350*. Inset charts summarise data from three independent biological replicates. Individual growth (B) and EC₅₀ (C, D) assays were carried out in triplicate and quadruplicate, respectively. Error bars represent standard deviation. *P*-values derived from Student's *t*-test (* <0.05; ** <0.01). RNAi inductions were carried out in 1 μ g.ml⁻¹ tetracycline.

Figure 8

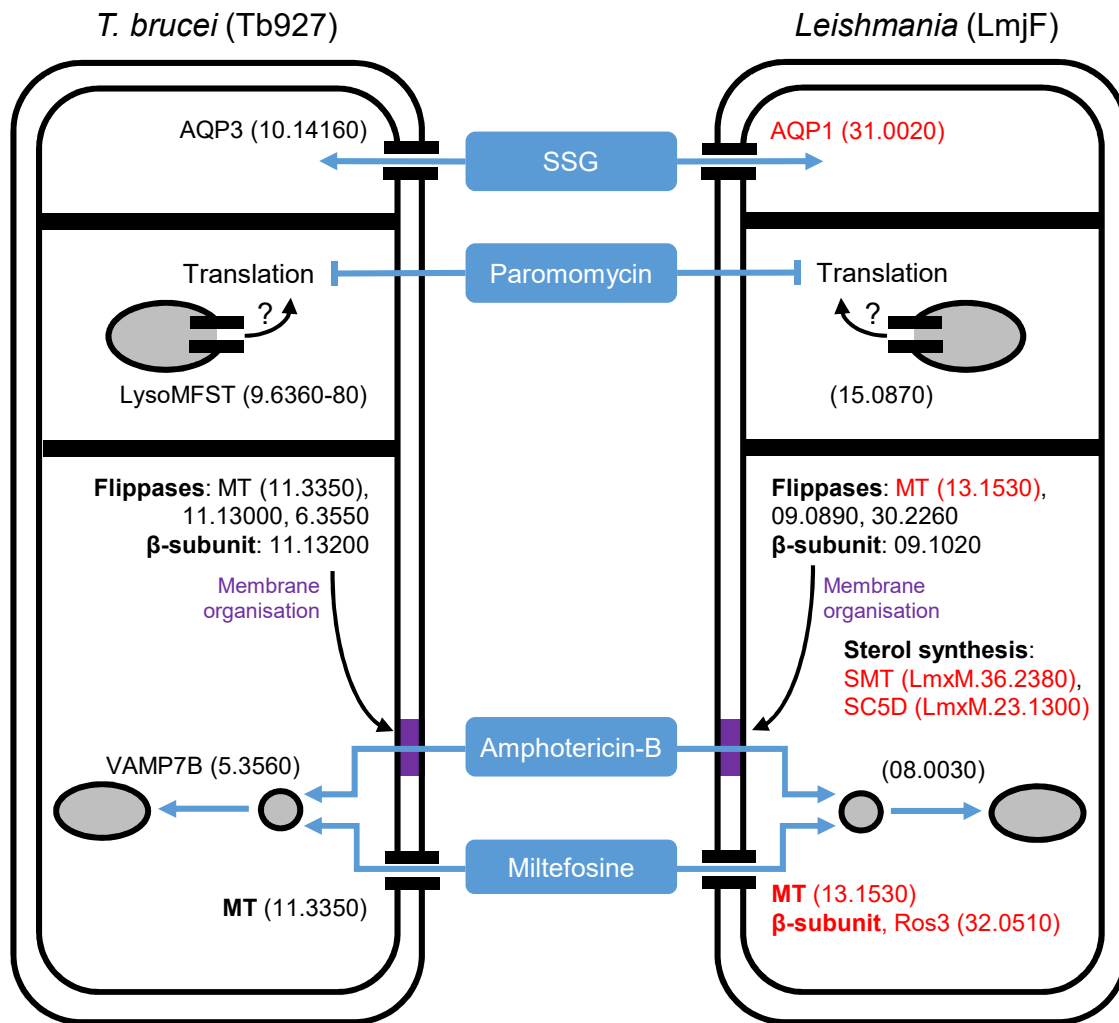
bioRxiv preprint doi: <https://doi.org/10.1101/605873>; this version posted April 13, 2019. The copyright holder for this preprint (which was not certified by peer review) is the author/funder, who has granted bioRxiv a license to display the preprint in perpetuity. It is made available under aCC-BY 4.0 International license.



Flippases influence the action of amphotericin-B. A) Neighbour joining phylogenetic tree showing the *T. brucei* and *L. major* flippases versus the *S. cerevisiae* flippases (Neo1p, Drs2p and DNF1-3) and a representative cation-transporting P-type ATPase (Pay2). Schematics of predicted *T. brucei* and *L. major* flippases and representative *S. cerevisiae* flippases (Neo1p and DNF3) and P-type ATPase (Pay2), highlighting key conserved residues (actuator domain: TGES [green triangle], DEGT [pink triangle]; and, phosphorylation domain, DKTGT [yellow triangle]); predicted signal peptide, vertical red bar; and, predicted *trans*-membrane domain organisation, vertical black bars. B) Total (red) and RNAi construct-specific 14mer-containing (blue) reads mapping to *Tb927.11.13000* and *Tb927.6.3550* following amphotericin-B selection. Targeted open reading frames highlighted in green; flanking open reading frames coloured grey. C) *T. brucei* population growth following RNAi knockdown of *Tb927.11.13000*. Inset: confirmation of RNAi knockdown by northern blot; ethidium bromide stained gel shown as a loading control. D, E) Representative amphotericin-B and miltefosine EC_{50} assays following RNAi knockdown of *Tb927.11.13000*. Inset charts summarise data from three independent biological replicates. Individual growth (C) and EC_{50} (D, E) assays were carried out in triplicate and quadruplicate, respectively. Error bars represent standard deviation. *P*-values derived from Student's *t*-test (* < 0.05; ** < 0.01). RNAi inductions were carried out in 1 $\mu\text{g}.\text{ml}^{-1}$ tetracycline, unless otherwise stated.

Figure 9

bioRxiv preprint doi: <https://doi.org/10.1101/605873>; this version posted April 13, 2019. The copyright holder for this preprint (which was not certified by peer review) is the author/funder, who has granted bioRxiv a license to display the preprint in perpetuity. It is made available under aCC-BY 4.0 International license.



Known and candidate drivers of anti-leishmanial drug efficacy in *Leishmania*. The key *T. brucei* proteins identified in our anti-leishmanial loss-of-function screen (left hand panel) and their *Leishmania* orthologues (right hand panel) represent candidate anti-leishmanial drug efficacy determinants. Red denotes known *Leishmania* drivers of anti-leishmanial efficacy whose loss-of-function reduces drug efficacy (see text for details). The strain prefix for the truncated gene IDs is at the top of each panel, with the exception of the sterol biosynthetic enzymes recently shown to contribute to amphotericin-B efficacy against *L. mexicana* [66]. Grey-filled circles (endosomes) and ellipses (lysosome) represent the endocytic system. The purple block represents membrane modified by changes in sterol biosynthesis and the putative action of the flippases and their β -subunit; changes in membrane composition anywhere in the endocytic system may influence the intracellular transit of amphotericin-B or its ability to form ion permeable channels.